UNIVERSITÀ DEGLI STUDI DI PADOVA

SCUOLA DI SCIENZE
Dipartimento di Geoscienze
Direttore: prof.ssa Cristina Stefani

TESI DI LAUREA MAGISTRALE
IN
GEOLOGIA E GEOLOGIA TECNICA

THE ROLE OF STRAIN-INDUCED MICROSTRUCTURES ON THE BULK EFFECTIVE SHEAR VISCOSITY: A NUMERICAL STUDY ON TWO-PHASE AGGREGATES

Relatore: *Prof. Manuele Faccenda*
Correlatore: *Prof. Giorgio Pennacchioni*

Laureanda: Giulia Fedrizzi

ANNO ACCADEMICO 2017/2018

Contents

1 Introduction

In this thesis, we want to investigate the role of a second phase in a polycrystalline aggregate deformed by simple shear with 3-D, high resolution numerical simulations. This second phase is dispersed in a rock matrix with different mechanical properties. We studied how the viscosity contrast, the volume fraction and the increasing applied shear strain affect the microstructure and, consequently, the bulk effective shear viscosity of the aggregate.

We discuss the shape of the inclusions and its evolution with strain as a simple shear deformation is applied to a cubical volume containing initially spherical inclusions dispersed in a matrix. The resulting microstructure evolves with strain and is a function of the viscosity contrast between the two phases and the volume fraction. Different microstructures cause different effective shear viscosities and therefore, the latter are a function of the same parameters too. We performed numerical simulations with both linear and power-law rheology.

1.1 Microstructures in polyphase aggregates

It is known that a polycrystalline rock undergoing a deformation does not deform homogeneously, but minerals with different rheologies respond differently to strain application. As a consequence, structures such as foliation and lineation can form even if the minerals were initially isodiametric. Microstructures in deformed rocks are a critical source of information on the rock's deformational history.

In the case of granitic rocks, for example, feldspars are relatively rigid phases, while micas are much more deformable. Consequently, when a shear deformation is applied, the more rigid clasts elongate and develop a prolate shape,

Figure 1: An example of foliated rock.

while micas and other weak phases accommodate more strain and form foliation planes (e.g. figure 1).

Much less is known about microstructures developing deeper in the Earth's interior. The geometry must depend on the rheology of each single phases in that type of aggregates as well.

1.2 Previous studies on two-phase aggregates

1.2.1 Hard sphere suspensions

Einstein's theoretical equation for the relative viscosity η_r of hard-sphere suspensions (Einstein, 1906) was the first that described the relative viscosity of hard-sphere suspensions as a function of the volume fraction of the spheres:

$$\eta_r = 1 + B\phi \tag{1}$$

where ϕ is the volume fraction and B is referred to as the 'Einstein coefficient'

or the 'intrinsic viscosity', (e.g. Mueller et al. (2010)) and depends on the particle shape. For rigid spheres, it takes the value $B = 2.5$ (Barnes, 2000). The equation, however, is only valid in the diluted regime, in the case of a single hard sphere in a fluid.

To account for interactions effects, higher-order volume-fraction terms can be added to Einstein's equation:

$$\eta_r = \eta_0(1 + B\phi + c\phi_2 + ...) \tag{2}$$

with c being a coefficient whose value has been calculated in many ways, depending on how many spheres interact with each other, on the spatial distribution function, etc.

Hsueh & Wei (2009) derived an equation for deformable spherical inclusions:

$$\phi = \phi_c \left(1 - \left(\frac{\eta_0}{\eta_r}\right)^{\frac{2}{5\phi_c}} \left(\frac{\eta_s - \eta_r}{\eta_s - \eta_0}\right)^{\frac{1}{\phi_c}}\right) \tag{3}$$

where ϕ is the volume fraction of rigid spheres, ϕ_c the densest possible packing for monodisperse spherical particles, η_0 and η_s the matrix and the sphere viscosity respectively. We compared this analytical solution with our initial value of the aggregate viscosity when the inclusions are still spherical in section 3.4.

Krieger and Dougherty's equation (4) is a semiempirical equation that gives the effective shear viscosity as a function of the inclusion volume fraction ϕ over the maximum inclusion volume in a concentrated regime (Krieger & Dougherty, 1959):

$$\eta_r = \left(1 - \frac{\phi}{\phi_c}\right)^{-B\phi_c} \tag{4}$$

This equation can also be seen as equation 3 when $\eta_s \to \infty$, that is when

the spheres are undeformable (rigid).

Theoretically, the densest possible packing for monodisperse spherical particles is $\phi_c \approx 0.74$. However, the maximum packing in disordered suspensions is typically lower: it is estimated to be between 0.64 (the value we used, by Rintoul & Torquato (1996)) and 0.68 (if additional structure is imposed by shear, Kitano et al. (1981)).

The equation is valid for a hard-sphere suspension, in which there are no interparticle forces other than infinite repulsion at contact (Genovese, 2012). The flow is dominated by hydrodynamic forces and the solid inclusion causes a hydrodynamical disturbance in the flow. This results in an increase in the viscosity due to an increase of the energy dissipation.

1.2.2 Experimental studies

Studying an aggregate that reproduces the lower mantle composition experimentally under lower mantle conditions is a great challenge, because of the difficulties in controlling the generation of stress and strain under high temperature and pressure (Karato & Weidner, 2008).

The first experimental study on the lower mantle composition and conditions was made by Girard et al. (2016), in which the authors studied the rheology of a bridgmanite-ferropericlase aggregate. The samples were made of 70% bridgmanite and 30% periclase.

As shown in figure 2, periclase is isolated in most cases, whereas bridgmanite appears to be interconnected. The MgO inclusions follow the finite strain ellipsoid (FSE) orientation: they start at an angle of 45° and progressively decrease their angle with the shear direction. This means that the periclase, which is the weak phase, accommodates more strain even if it is less abundant. The stronger phase, on the other hand, deforms much less and its FSE

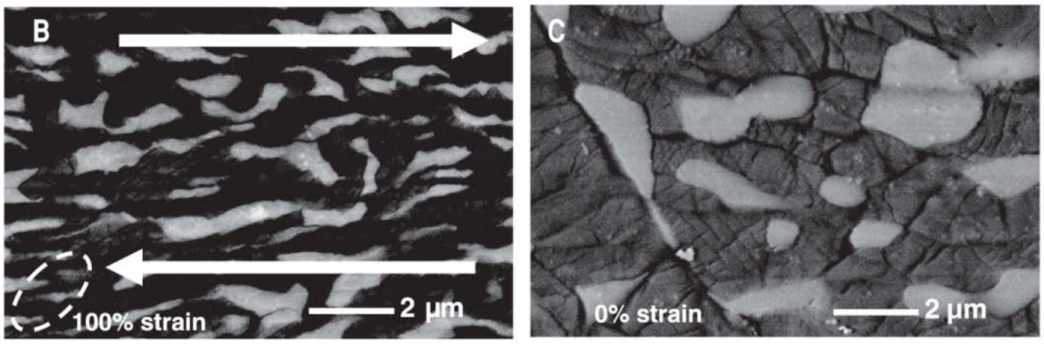

Figure 2: The deformation of a bridgmanite (dark gray grains) and ferropericlase (light gray grains) aggregate. Figure (B) shows the deformed sample after 100% of bulk strain together with an oblate ellipse showing the corresponding bulk strain ellipsoid. Arrows indicate the sense of shear. Figure (C) shows the same undeformed sample. SEM back-scattering images from Girard et al. (2016)

consequently rotates to a steeper angle with the shear direction with respect to the bulk strain ellipsoid. This shows that microstructures such as foliation already form at low strain.

Initially, the aggregate rheology is dominated by bridgmanite, but when periclase starts to interconnect, it forms foliation planes, along which strain can localise very easily. This causes an important weakening in the aggregate's rheology.

1.2.3 Models

Some models to describe the viscosity of two-phase aggregates have been proposed, including Handy (1994) and Takeda (1998). Handy (1994) described two types of microstructure that a polycrystalline aggregate can develop when subjected to simple shear. The study confirmed that the microstructure strongly depends on the rheologies of the phases that compose the aggregate. Mylonitic rocks and rock-analogue materials develop two main types of structure (Fig. 3): LBF (load-bearing framework) and IWL (intercon-

nected layer of a weak phase). The load-bearing framework includes a strong phase containing isolated pockets of a weak phase, whereas the interconnected layer of a weak phase separates clasts and boudins of a strong phase. Takeda

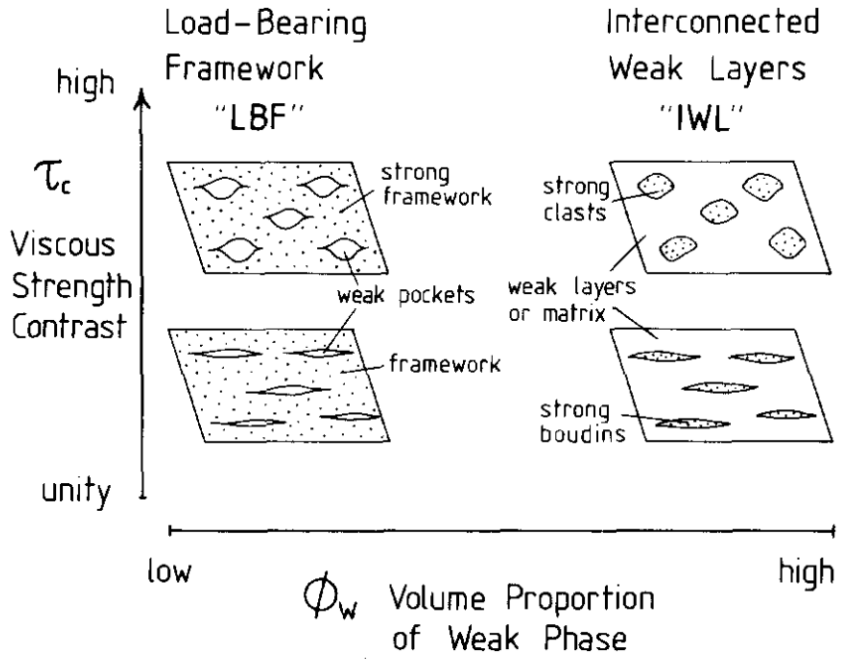

Figure 3: Handy's model for two-phase viscous materials. The weak phase volume fraction ϕ_w is reported in the horizontal axis, the viscosity contrast τ_c is represented in the vertical axis. From Handy (1994).

(1998) proposed two models for the Newtonian rheology, a linear relationship between the volume fraction and bulk viscosity of the aggregate when the rock has an LBF structure and a non-linear one when the aggregate shows an IWL structure. The first one is a linear combination of viscosities weighted by the volume fraction of their phases:

$$\mu^* = \phi_1 + b(1 - \phi_1) \tag{5}$$

while the second solution is more complex:

$$\mu^* = \frac{[a^2 - 2a(a-1)\phi_1 + (a-1)^2\phi_1^2]b}{a^2 + (b-a^2)\phi_1} \tag{6}$$

where $a = \rho_2/\rho_1$, $b = \mu_2/\mu_1$, ρ_1 and ρ_2 are the densities of the weak phase and the more viscous phase respectively, μ_1 and μ_2 are their viscosities, ϕ_1 is the volume fraction of the weak phase.

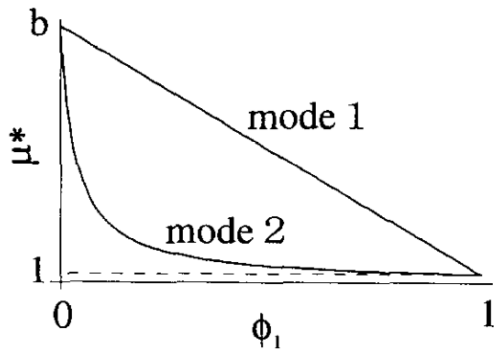

Figure 4: Takeda's equations predict two modes of behaviour. The first one is a linear relationship between the normalised bulk rock viscosity μ^* and the volume fraction of the weak phase ϕ_1. The second one is a non-linear relationship described by equation 6. From Takeda (1998).

According to the second equation, except for small volume fractions of the weak phase, the viscosity of a two-phase aggregate approximates the viscosity of the weaker component, as it is apparent from figure 4.

1.3 Motivation

1.3.1 Shear viscosity in a two-phase aggregate

The aim of this thesis is to study the effective shear bulk viscosity of a two-phase aggregate as a function of the viscosity contrast between matrix and

inclusions and of their volume fraction, and how the rheology and the microstructure evolve with increasing strain. The study focused on a two-phase material because, as described in section 1.3.2, most of the Earth materials are composed of two main phases or their behaviour can be approximated by a two-phases model. It is therefore most important to study how such aggregates respond to deformation. Their bulk viscosity cannot be computed by a simple weighted average of the two component's viscosity, because the microstructure strongly affects it.

There are a few studies about the rheology of two-phase aggregates, but none of them has shown the relationship that links bulk shear viscosity with shear strain, viscosity contrast and volume fraction.

Such an equation will have important applications in the field of geodynamic modelling. It will help predicting the variation of mantle viscosity with depth and strain caused by the microstructure development.

1.3.2 Mantle microstructure and bulk viscosity

Large-scale phenomena such as mantle convection cause the mantle materials to be deformed under plastic deformation, which leads to the development of microstructures when the material is not homogeneous.

The upper mantle is mainly composed of olivine and pyroxene. Their proportions depend on the mantle composition: olivine takes 60% of the volume in the case of a pyrolitic mantle, ∼75% for a harzburgitic one and ∼100% if the composition is dunitic. Since the second phase is almost entirely pyroxene, we can approximate the upper mantle to a two-phase aggregate. Pyroxene is the harder of the two minerals, therefore it is expected to develop poorly flattened but elongated grains.

Lower in the mantle, the pyroxene is progressively absorbed by garnet, there-

fore the composition changes into olivine polymorphs, Wadsleyite or Ringwoodite, and majoritic garnet in a 60:40 proportion in a pyrolitic mantle. Its strength appears not to be the same everywhere in the transition zone: in dry conditions, garnets are the strongest phase, but they become progressively weaker than olivine with increasing water content (Jin et al., 2001; Karato et al., 1995). In the first case, they are expected to assume elongated shapes as a consequence of the constrictional strain or behave like rigid inclusions, whereas in the second one, the garnets should undergo flattening.

At about 660 km depth, the post-spinel reaction occurs, which causes the decomposition of ringwoodite into bridgmanite and ferropericlase. Majorite progressively transforms to Ca- and Mg-perovskite and disappears at about 720-750 km (post-garnet reaction, Hirose (2002) and Stixrude & Lithgow-Bertelloni (2012), Faccenda & Dal Zilio (2017) for a review).

The viscosity of the lower mantle is a crucial parameter in geodynamic models because, since the lower mantle forms 65% of the whole Earth's mantle, it deeply affects the whole Earth's dynamics (Yamazaki & Karato, 2001).

The lower mantle is composed of (Mg,Fe)SiO_3 Bridgmanite ($\sim$70% by weight), (Mg,Fe)O Ferropericlase ($\sim$20%) and a small percentage of calcium perovskite $CaSiO_3$ (Ringwood, 1991). Ferropericlase is estimated to be three times weaker than Bridgmanite (Yamazaki & Karato, 2001), therefore it accommodates more strain and forms flattened crystals. Experiments on this type of aggregate were conducted by Girard et al. (2016), as described in section 1.2.2.

1.3.3 Boundary localisation

It has been often observed in nature that the deformation is not homogeneously distributed, but there is a localisation of strain at a boundary between two

rocks with different rheological properties (e.g. Pennacchioni & Mancktelow (2007)). Such localisation occurs in the weak rock when it is heterogeneous at the crystal scale, but is absent when the weaker rock is relatively homogeneous. This effect can be found at various scales in geological processes that involve simple shear deformation, so that localisation can be found, for example, (1) at the margin of a (weak) granodiorite intruded by a stronger aplite dike (Fig. 5) or (2) between two geological units at a much bigger scale, which causes the preservation of large low-strain domains because all the deformation is accommodated at the margins. Understanding the causes of this phenomenon might lead to an explanation of why low-strain domains are preserved (e.g. Bell et al. (1986)), while deformation is completely accommodated by shear zones situated at the unit margin, for example in the Tauern Window (Mancktelow & Pennacchioni, 2005).

What causes this phenomenon has not been explained in literature so far. Therefore, one of the goals of simulating the formation of microstructures is also to understand what may lead to this process.

Figure 5: An example of localisation at a boundary between granodiorite and an aplite dyke. The shear zone develops in the granodiorite, which is the weaker phase and has grain-scale heterogeneity. From Pennacchioni & Mancktelow (2007)

2 Numerical Methods

2.1 I3ELVIS

For the numerical simulation, we used I3ELVIS, a thermo-mechanical 3-D code developed by Taras V. Gerya for modelling geological flows (Gerya & Yuen, 2007). The code solves the equations of conservation of mass, momentum and energy, it uses a conservative finite difference scheme and a non-diffusive marker-in-cell technique to simulate multiphase flow (Moresi et al., 2003).

Although it was originally designed for simulations of geodynamic processes at the planetary scale, its set-up can be arranged for any initial geometry. This adapted version of the code is only mechanical and does not take into account temperature nor gravity.

The system has periodic boundary conditions: when a particle, because of its motion, arrives at a box boundary, it re-enters the box from the opposite side of the domain.

All the simulations have been performed with the *Cineca* computational facilities.

Figures and visualisation processes were made with *Paraview*, an open-source tool to visualise and analyse extremely large data sets (Ahrens et al., 2005; Ayachit, 2015).

2.2 Viscosity equations

We performed simulations in both Newtonian and non-Newtonian regimes. The shear viscosity for each phase is calculated as:

$$\eta_s = \eta_{s_0} \left(\frac{\dot{\varepsilon}_{II}}{\dot{\varepsilon}_{II_0}} \right)^{\left(\frac{1-n}{n}\right)} \tag{7}$$

with $\dot{\varepsilon}_{II_0} = 1$ and $n = 1$ for Newtonian and $n = 3$ for non-Newtonian rheology.

Thus, in the case of Newtonian regime it is possible to define a constant shear viscosity contrast:

$$\eta_c = \frac{\eta_{s_0,incl}}{\eta_{s_0,matr}} \tag{8}$$

where $\eta_{s_0,incl}$ and $\eta_{s_0,matr}$ are the intrinsic shear viscosity of the inclusions and the matrix respectively.

The effective shear viscosity of the bulk aggregate is calculated as:

$$\eta_{eff} = \frac{< \sigma_{II} >}{2 < \dot{\varepsilon}_{II} >} \tag{9}$$

where $< \sigma_{II} >$ is the average second stress invariant and $< \dot{\varepsilon}_{II} >$ is the average second strain invariant. The effective viscosity is then normalised to the reference matrix viscosity:

$$\eta_r = \frac{\eta_{eff}}{\eta_{s_0,matr}} \tag{10}$$

The bulk shear rate is defined as:

$$\dot{\gamma} = 2\dot{\varepsilon}_{xz} = 2\,\frac{1}{2}\left(\frac{\partial v_x}{\partial z} + \frac{\partial v_z}{\partial x} \right) \tag{11}$$

where $\partial v_x / \partial z$ is the difference in adimensional velocity between the top plate (-1) and the bottom plate (1) over the distance between the plates (0.9), whereas $\partial v_z / \partial x = 0$, because there is no imposed vertical velocity. Equation 11 can then be rewritten as:

$$\dot{\gamma} = \frac{-1 - (+1)}{0.9} = -2.\bar{2} \tag{12}$$

The bulk shear strain can be calculated from the shear rate by multiplying it with time:

$$\gamma = \dot{\gamma}\, t \tag{13}$$

2.3 Model setup

The setup includes 3 rock types: the inclusions, the rigid plates and the matrix. Their rheological properties are reported in table 1. The values of intrinsic shear viscosity can go from 1 to 50 (Newtonian regime) or from 1 to 10 (Non-Newtonian regime).

Table 1: Physical properties

	Newtonian	Non-Newtonian rheology		
Rock type	η_{s_0}	η_{s_0}	η_{min}	η_{max}
Inclusions	1-50	1-10	10^{-2}	10^{3}
Rigid plates	10^{4}	10^{4}	10^{4}	10^{4}
Matrix	1-50	1-10	10^{-2}	10^{3}

All quantities are dimensionless. In the non-Newtonian rheology, the contrast is in the pre-exponential factor η_{s_0} and the viscosity can assume values from $\eta_{min} = 10^{-2}$ to $\eta_{max} = 10^{3}$, depending on the strain rate.

In order to understand how microstructures evolve and how this affects the effective bulk viscosities of the aggregates, we varied two parameters and the rheological regime (Newtonian and power-law).

The first parameter that we studied was the contrast in intrinsic viscosity η_{s_0}. It is defined as the shear viscosity of the inclusions over the shear viscosity

of the matrix, in the simulations with Newtonian rheology and as the ratio between the pre-exponential factor in the simulations with non-Newtonian rheology (equation 8).

We considered values from $\eta_c = 0.02$ (inclusions 50 times weaker than the matrix) to $\eta_c = 50$ (inclusions 50 times stronger than the matrix). Values of contrasts greater than 50 or smaller than 0.02 in the Newtonian regime and greater than 10 or smaller than 0.1 in the non-Newtonian regime caused problems with the convergence of the model.

The second parameter that we considered is the volume fraction of the inclusions in the model. The box has volume 1 and 10% of its volume is occupied by the rigid plates. Of the remaining 0.9 volume, a fraction is taken by the inclusions and the rest by the matrix. Such fractions are 10%, 15%, 20%, 25% and 30%. Figure 6 compares the initial distributions of spheres that occupy 10% and 30% of the aggregate's volume.

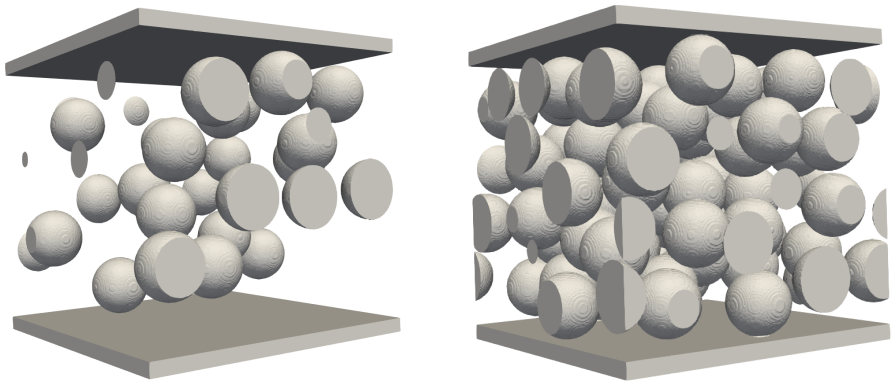

(a) 10% (b) 30%

Figure 6: Initial setups of the two end members for the volume fraction: 10% (left) and 30% (right).

2.3.1 Sphere distribution

The model for generating the initial position, size and shape of spheres in the matrix box is called GRADGENE3D, a code developed by Manuele Faccenda. The program randomly chooses a point in the available space and starts building a spherical volume around it. If the sphere radius reaches the imposed length, the inclusion position is saved; conversely, if the sphere touches another object before it reaches the set dimension, the inclusion is deleted and the program tries to build a new one from a different point.

The sphere radius can be fixed (Fig. 7a, monodisperse suspension) or belong to an interval (Fig. 7b, polydisperse suspension). In this case, the spheres radii varied between 0.05 and 0.2.

When the desired inclusions-to-matrix volume ratio is reached, the program saves the initial coordinates of all the spheres, which then have to be copied into the input file for the I3ELVIS code. The remaining volume is assigned to the matrix.

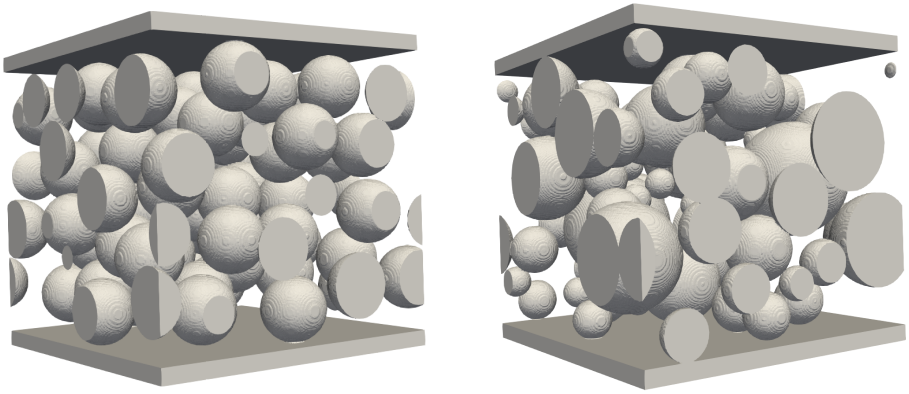

(a) Monodisperse (b) Polydisperse

Figure 7: Initial setups of the monodisperse and polydisperse suspensions with spherical inclusions and rigid plates. Here, the volume fraction of the inclusions is 30%.

2.4 Benchmark

In order to benchmark the code, we compared our numerical results of a single rigid sphere with two analytical solutions: Einstein's (Einstein, 1906) and Krieger and Dougherty's (Krieger & Dougherty, 1959) equations, described in section 1.2.1.

The numerical experiments performed to benchmark the code consisted of a single non-deformable sphere immersed in a matrix undergoing a simple shear deformation. This was imposed, like in the actual numerical experiments, by two sliding rigid plates at the top and bottom of the model. We performed tests with different radii, from 0.1 to 0.3. Two numerical resolutions were used, a lower one, with 101×101×101 nodes in each direction, and a higher one, with 245×245×245 nodes.

All the length and dimensions are normalised to the size of the box edge, which is set to one. Tests were performed both in Newtonian and non-Newtonian rheology.

To test the model, we computed the viscosity using two different equations, the first one involves the shear heating:

$$\eta_r = \frac{< h_s >}{(2 < \dot{\varepsilon}_{II} >)^2} \tag{14}$$

whereas the second one uses the second invariant of stress tensor:

$$\eta_r = \frac{< \sigma_{II} >}{2 < \dot{\varepsilon}_{II} >} \tag{15}$$

where η_r is the relative bulk shear viscosity, $< \cdot >$ are volume-averaged quantities in the matrix-inclusion domain, $< h_s >$ the mean shear heating, $< \dot{\varepsilon}_{II} >$ the mean second invariant of the strain rate tensor and $< \sigma_{II} >$ the mean second invariant of the stress tensor.

Our results perfectly reproduced the values predicted by the Krieger and Dougherty's equation (eq. 4) if the viscosity was calculated using equation 15. The results were more accurate when they were performed with high numerical resolution. The effective viscosity results from all tests with all the different radii are shown in figure 8, together with the comparison with the two analytical solutions (equations 1 and 4).

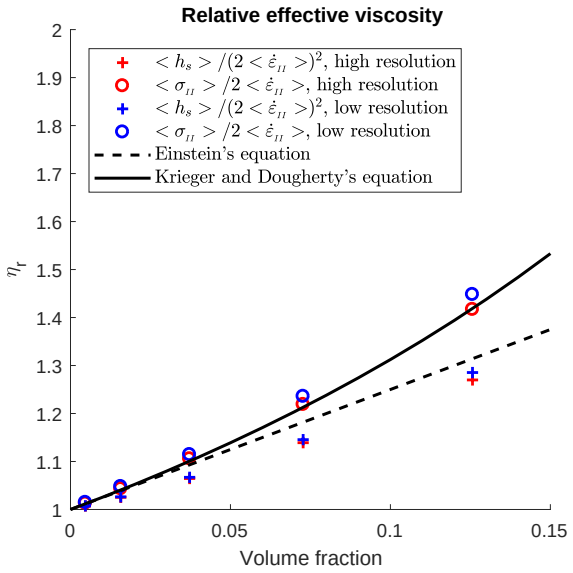

Figure 8: Relative effective viscosity of a hard-sphere suspension as predicted by Enstein's and Krieger and Dougherty's equations, dashed and solid lines respectively, and as computed by our model, using two different equations and two resolutions. Newtonian regime.

We report the dynamic variables fields from the third of our benchmark experiments, in which the spherical inclusion had a radius of 0.2, in figure 11. The model produced symmetrical geometries in the several computed variables, which is what one can expect from such set-ups.

The velocity field is perturbed around the sphere by its presence. The matrix flow is hindered by the rigid inclusion in the central part of the model, which

causes the velocity to be higher at the top and bottom of the sphere, where the flow is stronger.

Higher values in the vorticity field are found at the top and at the bottom of the inclusion, whereas low values are located in the regions of low velocity.

A comparison between the velocity field in a Newtonian and in a non-Newtonian regime is reported in figure 9. The model dimensions are too small to tell if the separatrix is bow-tie-shaped or eye-shaped, in fact it is not possible to see the stagnation points and the shape of the stramlines around them. Nevertheless, there doesn't seem to be much difference between the two regimes, which is consistent with Pennacchioni et al. (2000).

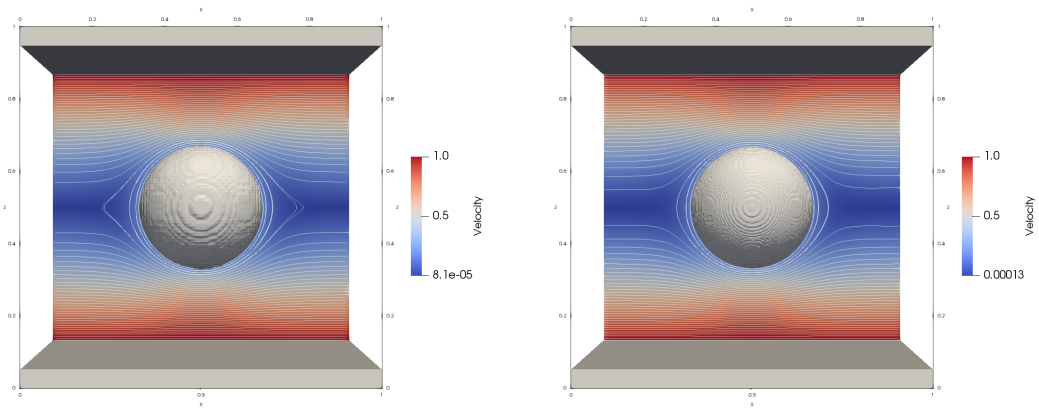

(a) Newtonian (b) Non-Newtonian

Figure 9: Streamlines and velocity field in a matrix containing a rigid (non-deformable) sphere. The sphere's radius is 0.2. The viscosity contrast is $\eta_c = 1000$.

Stress and second invariant of strain rate are both perfectly symmetrical, with maxima and minima positioned around the sphere.

Strain is not symmetrical because it accumulates while the inclusion rotates, entraining part of the matrix in its motion.

A vertical section displaying the pressure distribution shows four quadrants, two positive and two negative. The two positive ones are in the σ_1 direction. The pressure perturbations generated by a rigid sphere are compared with the ones predicted by the 2-D analytical solution by Schmid & Podladchikov (2003) in figure 10. The presence of a rigid sphere embedded in a matrix 1000 times weaker leads to two zones of overpressure and two of underpressure, symmetrically distributed in four quadrants. In our case, because the shear is sinistral, the main component of stress is in the second and fourth quadrants, in Schmid & Podladchikov (2003), it is in the first and third ones, being in a dextral simple shear situation.

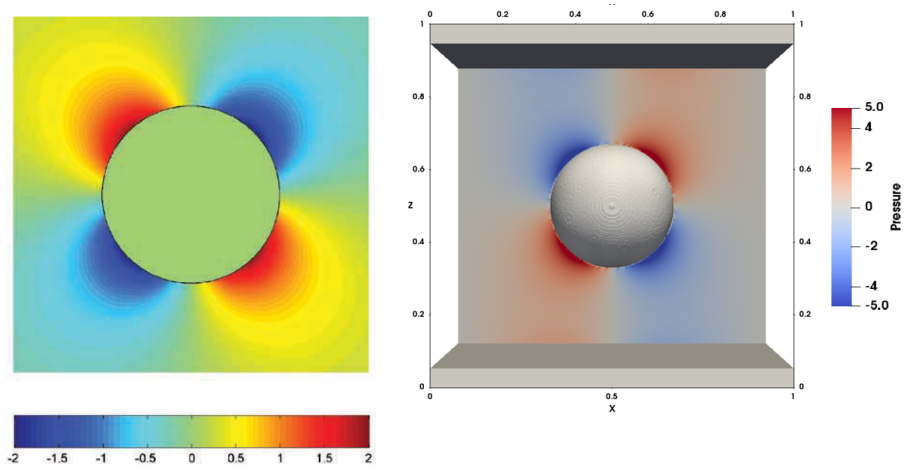

Figure 10: Pressure distribution in Schmid & Podladchikov (2003) and in our benchmark experiment. The first distribution is caused by a dextral simple shear, the one in our model by a sinistral simple shear.

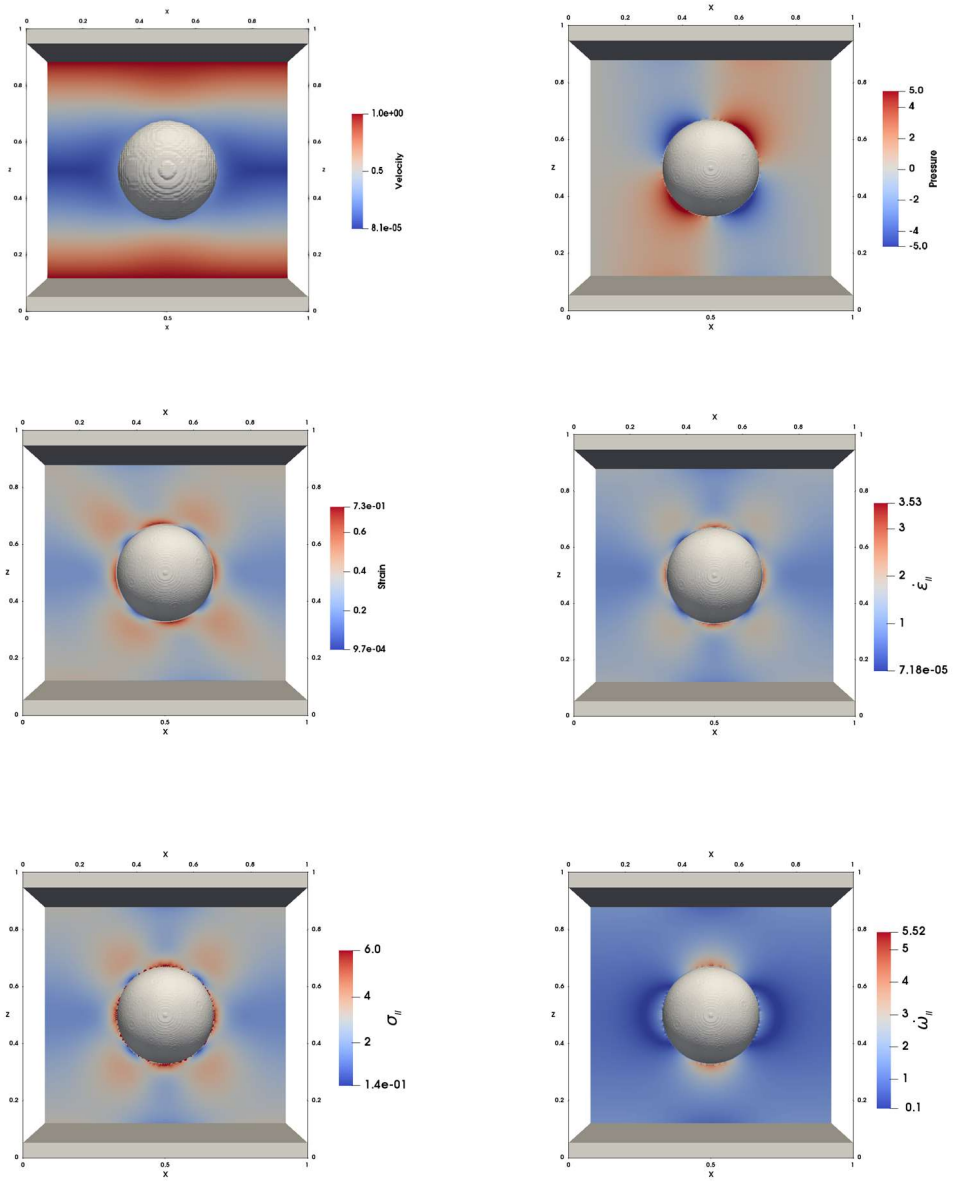

Figure 11: A single rigid sphere is immersed in a deformable matrix. A vertical plane positioned at half the length of the y axis shows velocity, pressure, strain, second invariant of the strain rate, second invariant of stress and second invariant of vorticity of the matrix. The rheology is Newtonian.

2.5 Post processing

We wanted to track the evolution of the microstructure with some parameters in order to evaluate it in a more precise way. It is interesting to see how some of the variables change along the vertical direction when the strain increases. Therefore, the post processing included some calculations about the inclusions shape and position. It also allowed us to assign a mean value of strain rate and vorticity to each inclusion in a vertical profile.

We used D-Rex, a program written in Fortran 90 that was developed for simulating LPO evolution, initially for olivine aggregates, then expanded to other minerals, by plastic deformation and dynamic recrystallisation (Kaminski et al., 2004).

The program takes as input the velocity gradient tensor $D_{ij} = \partial v_i / \partial x_j$ and the initial position of the inclusions, as provided by GRADGENE3D (section 2.3.1). The finite strain ellipsoid (FSE), the strain rate and vorticity of the inclusions are obtained by averaging these quantities from all the particles belonging to a given inclusion.

The aspect ratio is defined as the ratio of the long axis over the short axis of a particle: $R = a_1/a_3$.

With this output, for each inclusion it is possible to plot as a function of the bulk shear strain:

- The ratio of FSE's semi-axes on a Flinn diagram
- The aspect ratio
- The average strain rate
- The average vorticity

2.6 Fitting

In order to find an equation for the bulk effective shear viscosity as a function of shear strain, viscosity contrast and volume fraction, the data of the effective viscosity had to be fitted with a least square regression to a curve. The problem involves four dimensions, since there are three independent variables and one dependent variable. However, it is possible to split the problem into two phases. In the first fit, the effective shear viscosity is parametrised as a function of strain and some coefficients that depend on volume fraction and viscosity contrast. The coefficients are then modelled as a function of the two other parameters as 2-D surfaces.

All the data processing after the numerical experiments was performed with MATLAB. Fitting has been made with the *lsqcurvefit* function, a solver for non-linear data-fitting problems in least-square sense. Given two input dataset ($xdata$, $ydata$) and a function, the solver calculates coefficients (c) that solve:

$$\min_x \|F(c, xdata) - ydata\|_2^2 = \min_x \sum_i (F(c, xdata_i) - ydata_i)^2.$$

It minimises the sum of the squares of the residuals of the points from the curve described by the function F and its coefficients c. The algorithm proceeds iteratively from an initial guess until the error is less the function tolerance, the change in the coefficients or residuals is less than the tolerance or the maximum number of iterations is reached (*MATLAB Optimization Toolbox*).

The goodness of fit is evaluated with the coefficient of determination (R^2). It is a statistical measure of how well the model predicts the real data and it is calculated as the square of the Pearson's correlation coefficient ($\rho_{Y,\hat{Y}}$) between the data and the model, which is computed as:

$$\rho_{Y,\hat{Y}} = \frac{\mathrm{cov}(Y, \hat{Y})}{\sigma_Y \sigma_{\hat{Y}}}. \tag{16}$$

This expression can be rewritten so that

$$\rho(Y, \hat{Y})^2 = \frac{\sum_i (\hat{Y}_i - \bar{Y})^2}{\sum_i (Y_i - \bar{Y})^2} \tag{17}$$

which can be proved to correspond to the definition of R^2:

$$\rho(Y, \hat{Y})^2 = \frac{SS_{reg}}{SS_{tot}} = R^2 \tag{18}$$

where Y and $\hat{Y}$ are the observed and the predicted data respectively, σ_Y, $\sigma_{\hat{Y}}$ are their standard deviations, SS_{reg} is the total sum of squares and SS_{tot} the explained sum of squares.

3 Results

3.1 Newtonian Rheology

3.1.1 Fabric

The aggregate's fabric evolved with increasing strain with geometries that depend on the viscosity contrast and on whether the rheology was Newtonian or not. Our simulations reached shear strain $\gamma = 10$.

We observe two completely different fabrics if the inclusions were less viscous or more viscous than the matrix. The evolution of the fabric can be found at the link in figure 12, where 12a has $\eta_c = 0.1$ and 12b $\eta_c = 10$, while the fabric at $\gamma = 10$ is shown in figures 13 and 15 respectively.

Inclusions weaker than the matrix become oblate, flatten out and eventually merge. They form planes of interconnected weak material that spread throughout the whole aggregate width (Fig. 13).

In general, inclusions stronger than the matrix develop an elongated shape like a prolate ellipsoid. Some of them tend to aggregate too, but they never form pervasive planes (Fig. 15). However, for small viscosity contrasts (e.g. $\eta_c = 2$), even if they are stronger than the matrix, some flattening occurs in the inclusions, leading to a microstructure that is between the two end members. In this case, the inclusions slightly flatten out, but rarely merge (Fig. 14).

(a) `https://goo.gl/GHpzXB` (b) `https://goo.gl/zpCSbg`

Figure 12: Animations showing the evolution of fabrics for $\eta_c = 0.1$ (a) and $\eta_c = 10$ (b).

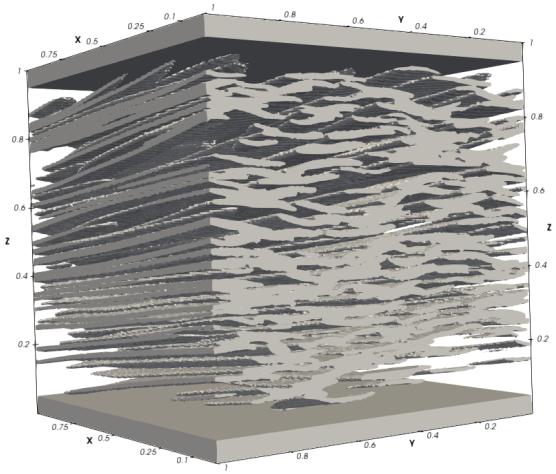

Figure 13: Inclusions shape in an aggregate after $\gamma = 10$. Inclusions viscosity is 10 times lower than the matrix viscosity.

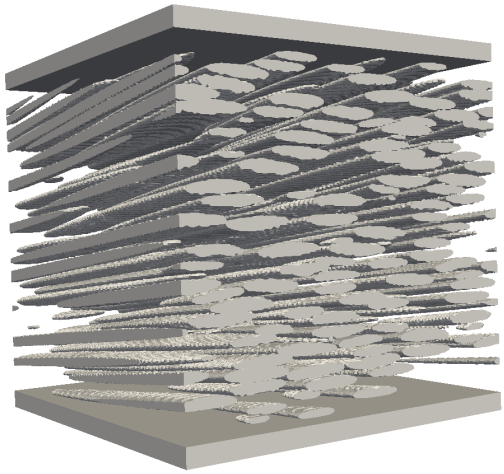

Figure 14: Inclusions shape in an aggregate after $\gamma = 10$. Inclusions viscosity is 2 times higher than the matrix viscosity.

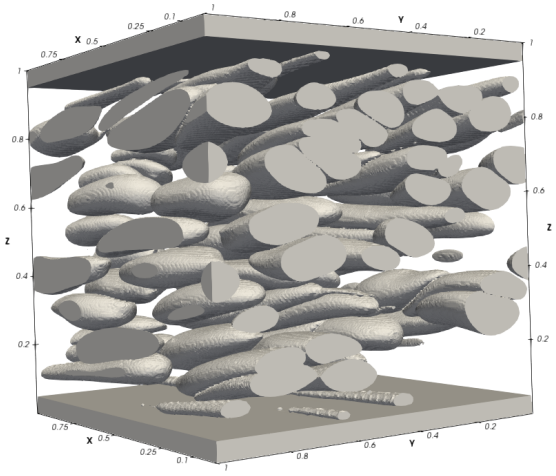

Figure 15: Inclusions shape in an aggregate after $\gamma = 10$. Inclusions viscosity is 10 times higher than the matrix viscosity.

We used three ways of tracing the evolution of the microstructure and the shape and position of each inclusion that forms it: Aspect ratio, their height above the lower plate and where they plot on the Flinn diagram.

A good indicator of how the microstructure evolves with strain is the aspect ratio of the inclusions. Calculated as the ratio of the longest axis over the shortest, it is plotted as a function of the distance from the lower plate in figure 16. Each point represents an inclusion and its coordinate in the y axis shows its position along the vertical axis (z in the models). The inclusions start from a spherical shape (aspect ratio = 1) and elongate with the progressive application of strain. In the case of strong or weak inclusions, the evolution of the aspect ratio is similar: inclusions are more elongated closer to the boundaries in both cases, but they differ at the beginning and in absolute values. In aggregates with weak particles, the inclusions are more elongated

at the centre of the model when the deformation process starts and only after some strain application this configuration changes and the inclusions are more elongated at the boundaries. The values reached at $\gamma = 10$ are almost four orders of magnitude greater than the initial ones. The difference between the ellipticity of the inclusions at the margins and the ones at the center is almost of two orders of magnitude.

When inclusions are stronger, the aspect ratio distribution does not change its pattern. It starts with higher values at the boundaries and preserves this concavity while the strain increases. The values are not as high as in the previous case: the highest ones are around 12 and the central ones are approximately half this value and not orders of magnitude lower as it happens in the weak inclusions.

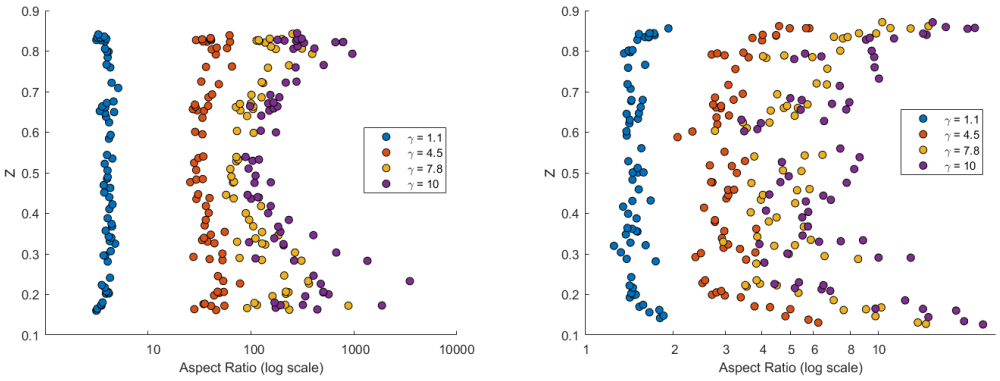

(a) $\eta_c = 0.1$ (b) $\eta_c = 10$

Figure 16: Aspect ratio evolution with increasing strain of weak and strong inclusions in aggregates with viscosity contrasts $\eta_c = 0.1$ and $\eta_c = 10$. Inclusions are 30% of the aggregate's volume.

If we approximate the inclusions' shape to an ellipsoid, it is possible to plot it on a Flinn diagram and evaluate whether the inclusions evolve into prolate or oblate ellipsoids. The shape of an initially spherical inclusion reflects its finite

strain ellipsoid. The longest distance between two points of the inclusion is taken as the longest axis (a_1), and two perpendicular directions as a_2 and a_3, with a_3 being the shortest. They represent the principal strain axes and were initially diameters of the sphere. The ratio between the longest and intermediate axes, a_1/a_2, of each inclusion is plotted along the y axis, whereas the ratio between the intermediate and shortest axes, a_2/a_3, is plotted along the x axis. Therefore, the shape of each ellipsoid can be fully characterised by these two ratios.

Points that plot on the diagonal have the intermediate axis that remains constant during deformation and the white circle represents the shape of the bulk ellipsoid. This would be the position of the points if the material was homogeneous and the strain plane. Our aggregates, however, are characterised by inclusions with a different viscosity with respect to the matrix. This results in a non-homogeneous distribution of strain that causes a different deformational behaviour between matrix and inclusions. Therefore, most of the points that represent the inclusions plot away from the diagonal line.

In the region below the diagonal line plot the inclusions that undergo flattening strain. They have an oblate shape and the intermediate axis is longer than the original sphere radius.

In the case of constrictional strain, the ellipsoids have a prolate shape and plot above the plane strain line. These are the spheres that shorten their intermediate axis.

After a deformation of $\gamma = 10$, aggregates whose inclusions are more viscous than the matrix have their inclusion ellipsoids plotted above the diagonal line (Fig. 17a). The inclusions are less deformed than the bulk aggregate: in fact, the ellipsoids are closer to the axes origin than the white sphere representing the bulk deformation.

If the viscosity is lower in the inclusions, they accumulate more strain and plot much farther from the origin and below the diagonal line. Therefore, we can conclude that they are much more deformed and assume an oblate shape (Fig. 17b).

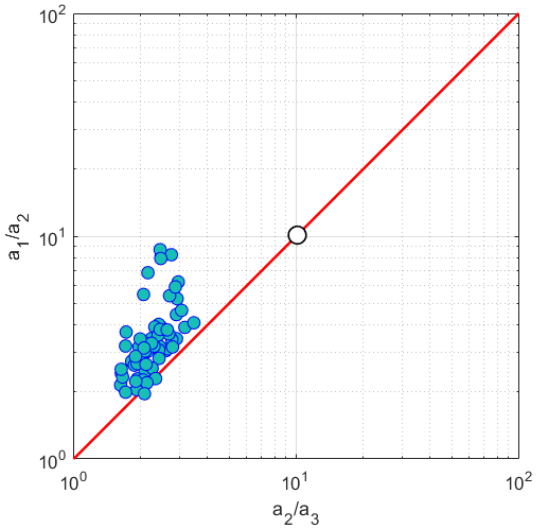

(a) $\eta_c = 10$

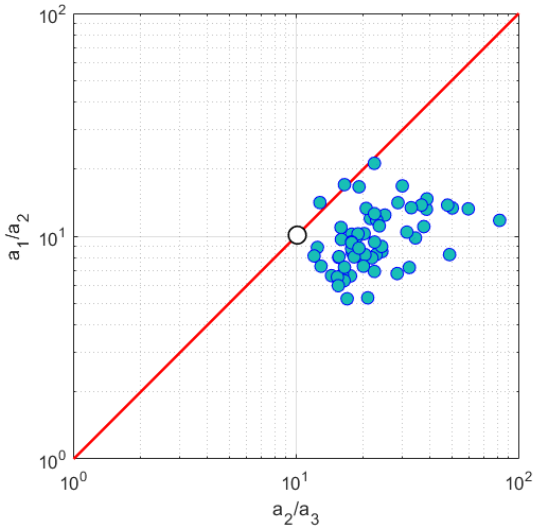

(b) $\eta_c = 0.1$

Figure 17: Flinn diagram of aggregates with $\eta_c = 10$ and $\eta_c = 0.1$ respectively. Newtonian rheology, volume fraction $\phi = 30$ in both figures.

The last way we used to trace the microstructure evolution is the height of each inclusion as a function of the shear strain. Figure 18 shows the vertical coordinate of the centre of each inclusion plotted against the shear strain (γ). The result is a graph that describes the variation of each inclusion's position along the vertical axis with time.

For $\eta_c << 1$, inclusions that are closer to the plates tend to migrate away from the boundaries. This is a well-known phenomenon in fluid dynamics: particles in a flow tend to concentrate at the center of the flow and away from the margins. Our inclusions, as initially passive elements, take this behaviour.

For $\eta_c >> 1$, however, they show the opposite behaviour and get closer to the rigid plates, as they tend to move towards regions that are free from inclusions, such as the zones close to the plates. The vertical coordinate of each inclusion oscillates as they are pushed by the neighbouring inclusions towards the plates. This effect is more visible at low strains, when the particles are still nearly spherical. It is also more efficient when the volume fraction is higher and particularly when the viscosity contrast is greater. As in the case of weaker inclusions, the oscillations are greater at the incipient phase of deformation, but they do not disappear as the strain increases, at least not before it has reached $\gamma = 10$. Some symmetrical trends can be observed when two inclusions are interacting with each other: while a curve decreases, another one increases. The correspondence between trajectories is, however, not perfect, as the interaction is not limited to two inclusions at a time, but they are affected by the presence of other surrounding particles. These multiple interactions make the curves more variable and complicated.

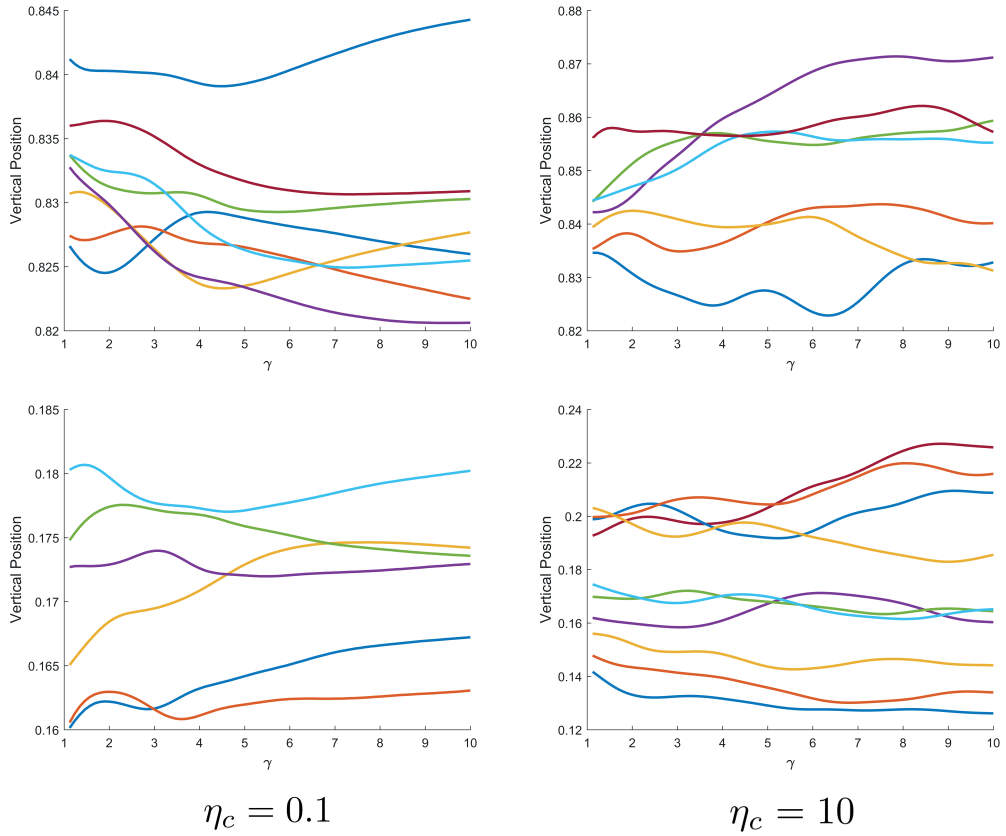

Figure 18: Vertical positions of inclusions closest to the boundaries with the increase of γ. On the left side, the viscosity contrast is 0.1, on the right side, $\eta_c = 10$. On the y axis, their distance from the bottom of the model is reported.

In polydispersed suspensions, weak inclusions interconnect more easily. Suspensions with the same volume fraction of the less viscous phase but with inclusions that have different dimensions are more likely to develop foliation planes. Since the inclusions accommodate much more strain when they are interconnected, the difference in strain distribution between inclusions and matrix is higher in polydispersed aggregates (Fig. 19a). This phenomenon is

emphasised in the power-law regime (Fig. 19b), where this difference in inclusions dimensions leads to the formation not only of interconnected planes, but also of S-C structures.

In fact, the most efficient way to make the weak inclusions interconnect is having a power-law viscosity. The fact that they accommodate more strain causes them to lower their viscosity, which makes it easier and easier for them to deform. The localisation mechanism is so efficient that they form S-C planes that are as wide as the model width.

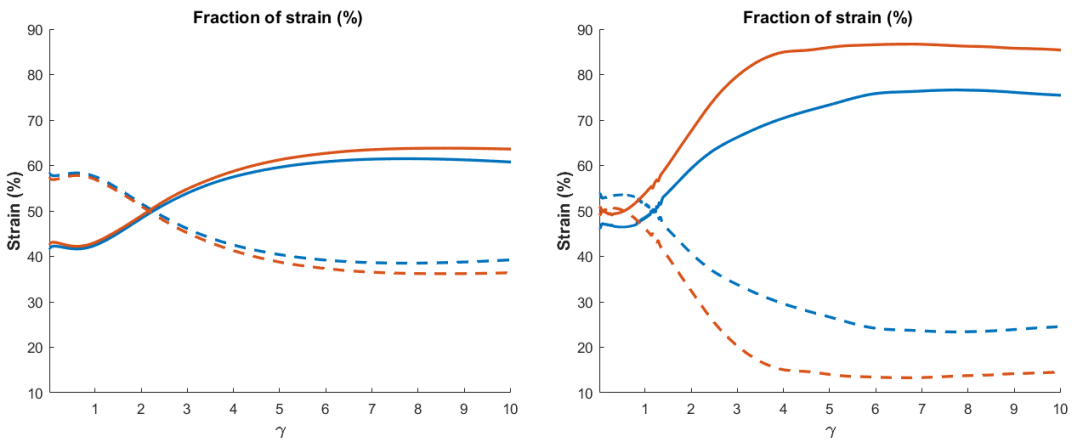

(a) Newtonian rheology

(b) Non-Newtonian rheology

Figure 19: Comparison between monodispersed suspensions and polydispersed suspensions in Newtonian and power-law regime. Red and orange lines are the strain evolution of polydispersed suspensions, blue lines are monodispersed suspensions. Solid lines are the strain evolution in the matrix, dashed lines strain evolution in the inclusions.

3.1.2 Dynamic Variables Fields

In this section, we report the distribution of strain, pressure, stress, strain rate, vorticity and velocity along a vertical plane positioned at the middle of the model, perpendicular to the y axis, and parallel to the deformation direction (x axis) and the vertical one (z axis). In the reported simulations, the viscosity contrast η_c is 10, when the inclusions are the more viscous phase, and $\eta_c = 0.1$, when the matrix is. In all the following aggregates, inclusions occupy 30% of their volume. All the figures have been made at $\gamma = 10$.

Strain.

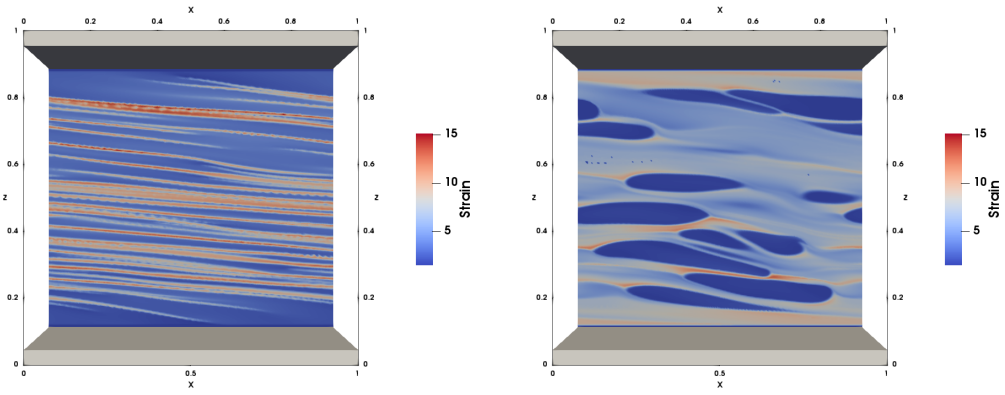

(a) $\eta_c = 0.1$ (b) $\eta_c = 10$

Figure 20: Strain distribution for inclusions 10 times weaker (a) and 10 time stronger (b) than the matrix.

Strain localises in the inclusions if they are weaker than the matrix, which barely deforms. The more interconnected they get, the more strain localises in them, forming foliation planes. This is particularly evident in the inclusions

that have merged at ~ 0.8 along the z axis (Fig. 20a).

In the second case, the inclusions accumulate much less strain, which is concentrated mainly in the matrix around them instead (Fig. 20b). The volume between two strong inclusions is the place where strain accumulation is more favoured, followed by the portions of matrix closest to the plates.

Pressure.

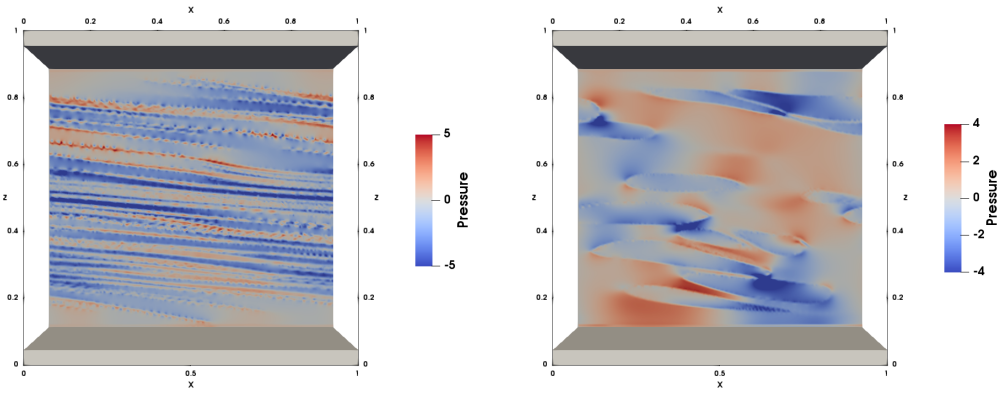

(a) $\eta_c = 0.1$ (b) $\eta_c = 10$

Figure 21: Pressure distribution for inclusions 10 times weaker (a) and 10 time stronger (b) than the matrix.

The pressure distribution in inclusions and matrix is consistent with the distribution that Moulas et al. (2014) described in with their analytical solutions. In our case, a sinistral simple shear deformation is applied along the x direction by the plates. Therefore, σ_1, the main component of stress, is at an angle of 45°, which means that it is nearly perpendicular or at a high angle to the inclusions.

Higher or lower pressure develop in an inclusion according to its viscosity (Fig. 22) and to the stress geometry. Under compressive conditions, with σ_1 perpendicular to the longest axis, a weak elliptic inclusion immersed in a stronger viscous matrix has a higher pressure and stress inside the inclusion than in the matrix. The opposite configuration develops if the inclusion is stronger, causing it to have a negative pressure with respect to the matrix (Moulas et al., 2014). The same pattern of pressure distribution is observed in our models, which have the principal direction of stress nearly perpendicular to the inclusion longest axes. However, the pressure distribution described in figure 22 is true for an isolated and perfectly elliptical inclusion. In fact, the pressure in our simulations is not at all as regular as in the analytical solution of a single 2-D ellipse. Despite the complexity of our model, what Moulas et al. (2014) predicted is generally valid in our aggregates.

Positive pressure is found inside the inclusions when they are weaker. The places with the lowest pressure are the matrix regions closest to the inclusions tips, forming zones of underpressure parallel to the direction of the inclusions elongation. In the case of stronger inclusions, pressure is generally higher in the matrix, especially at the boundary between matrix and an inclusion when this is perpendicular to σ_1 and there are no interactions with other particles. In case such interactions occur, pressure localises between the inclusions: the closer two inclusions are, the higher the pressure between them will be. Pressure is negative inside the inclusions, but it is not homogeneous due to their irregular shape and to the interactions between them.

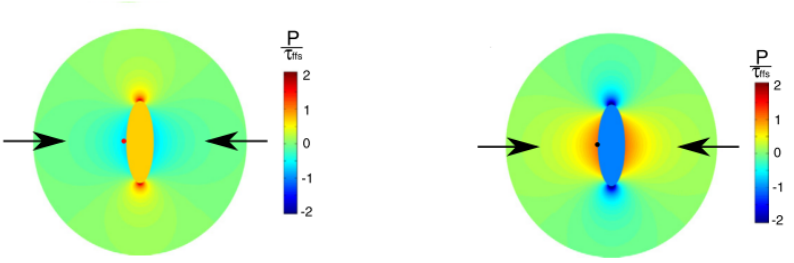

(a) Weaker inclusion (b) Stronger inclusion

Figure 22: Pressure field perturbation in a viscous medium due to an elliptical inclusion predicted by analytical solutions. From Moulas et al. (2014).

Stress.

In figure 24a, the stress distribution is almost homogeneous because the inclusions are not obstacles to the matrix flow any more. They don't localise stress except for very small regions. However, if the inclusions are stronger (Fig. 24b), there is still some localisation where two inclusions are very close to each other. They are places in which the matrix flow is more obstructed.

However, the stress field is not constant at all during the deformation process. This is particularly evident in the case of high viscosity contrasts, as observed from figure 23. Stress progressively assumes more extreme values and concentrates much more in the matrix at higher viscosity contrast. This phenomenon is known as stress concentration and causes a hinder in the flow of the matrix, which is the load-bearing framework. As strain increases, the difference in stress field amongst aggregates with different viscosity contrasts becomes smaller.

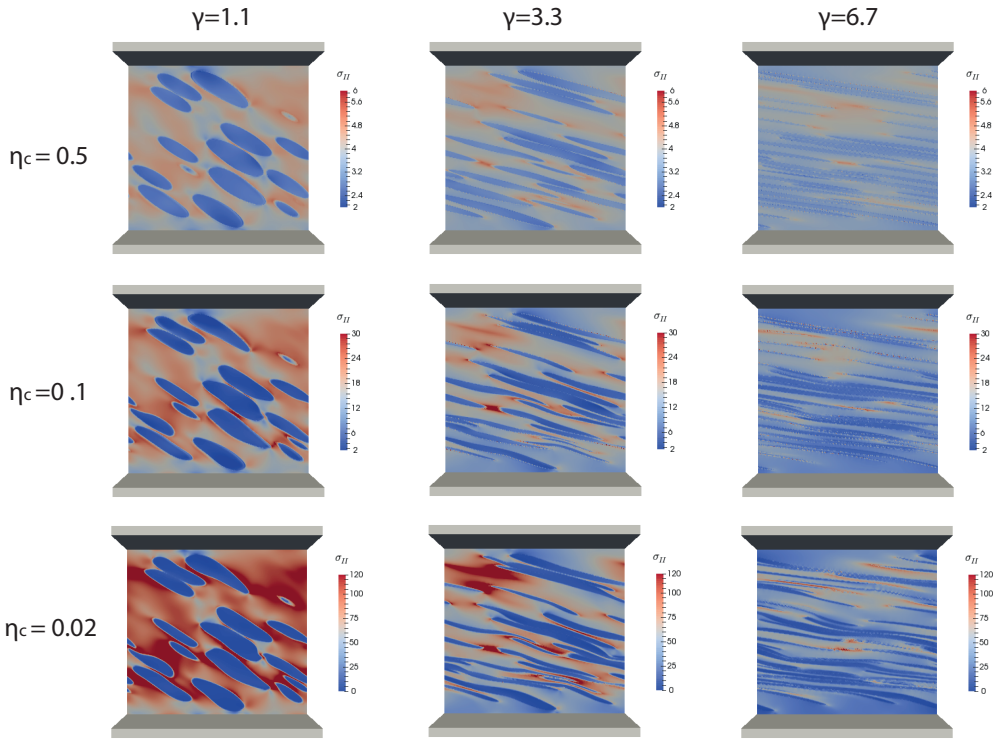

Figure 23: Stress evolution with strain for three different viscosity contrasts.

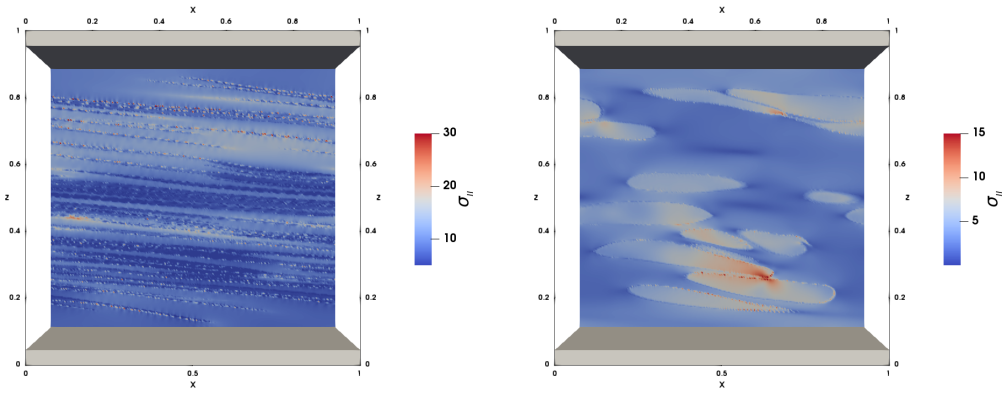

(a) $\eta_c = 0.1$ (b) $\eta_c = 10$

Figure 24: Stress distribution for inclusions 10 times weaker (a) and 10 time stronger (b) than the matrix at $\gamma = 10$.

Strain rate.

Strain rate distribution shows how inclusions are accommodating more and more strain when the inclusions are less viscous (Fig. 25a). The effect is greater once they have merged with each other, because it is along these planes that deformation can localise more easily. A higher strain rate in such planes means that deformation is still increasing. In the opposite configuration, inclusions deform very little, especially in the last steps (Fig. 25b). Strain is still increasing in the portions of matrix between two inclusions close to each other, especially when their margins are parallel to the matrix flow.

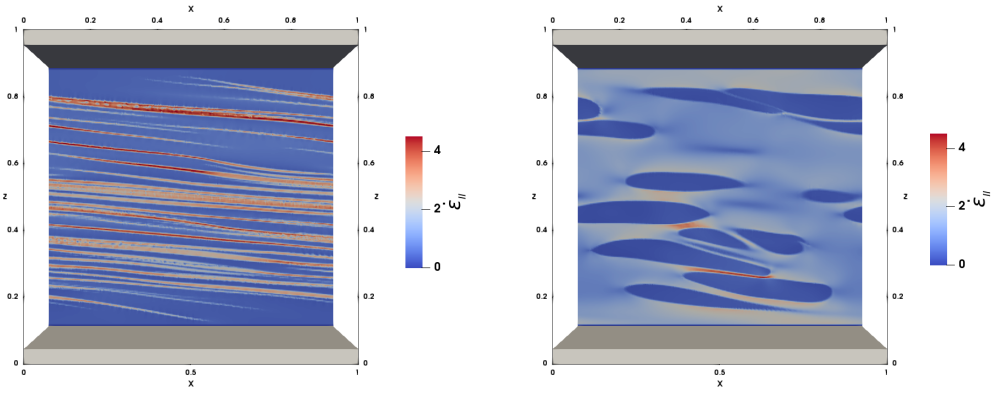

(a) $\eta_c = 0.1$ (b) $\eta_c = 10$

Figure 25: Second invariant of strain rate distribution for inclusions 10 times weaker (a) and 10 time stronger (b) than the matrix.

Vorticity.

At $\gamma = 10$, the vorticity distribution (Fig. 26) resembles the strain rate one. It is higher in the weaker phase, especially where the inclusions merge ($\eta_c = 0.1$) or where the matrix is confined by two neighbouring strong inclusions ($\eta_c = 10$). The similarity is caused by the fact that their main components are

the xz components, which are defined as:

$$\dot{\varepsilon}_{xz} = \frac{1}{2}\left(\frac{\partial v_x}{\partial z} + \frac{\partial v_z}{\partial x}\right)$$

and

$$\dot{\omega}_{xz} = \frac{1}{2}\left(\frac{\partial v_x}{\partial z} - \frac{\partial v_z}{\partial x}\right)$$

and the vertical component of the velocity field v_z is negligible compared to the horizontal one (v_x). Therefore, the two xy components $\dot{\varepsilon}_{xz}$ and $\dot{\omega}_{xz}$ are almost the same.

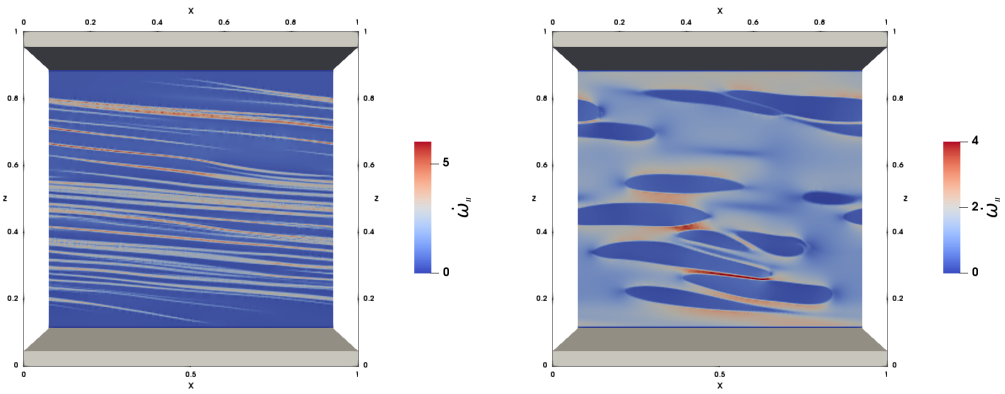

(a) $\eta_c = 0.1$ (b) $\eta_c = 10$

Figure 26: Second invariant of vorticity distribution for inclusions 10 times weaker (a) and 10 time stronger (b) than the matrix.

Although the two parameters reach very similar values, they do not start with the same ones and they have different evolutions with the shear strain. In fact, if we plot them on a 1-D diagram in which the inclusions have been sorted by their vertical position, they show a different evolution, which is reported in figure 27 for an aggregate with $\eta_c = 0.1$. At low strain, the vorticity is lower in

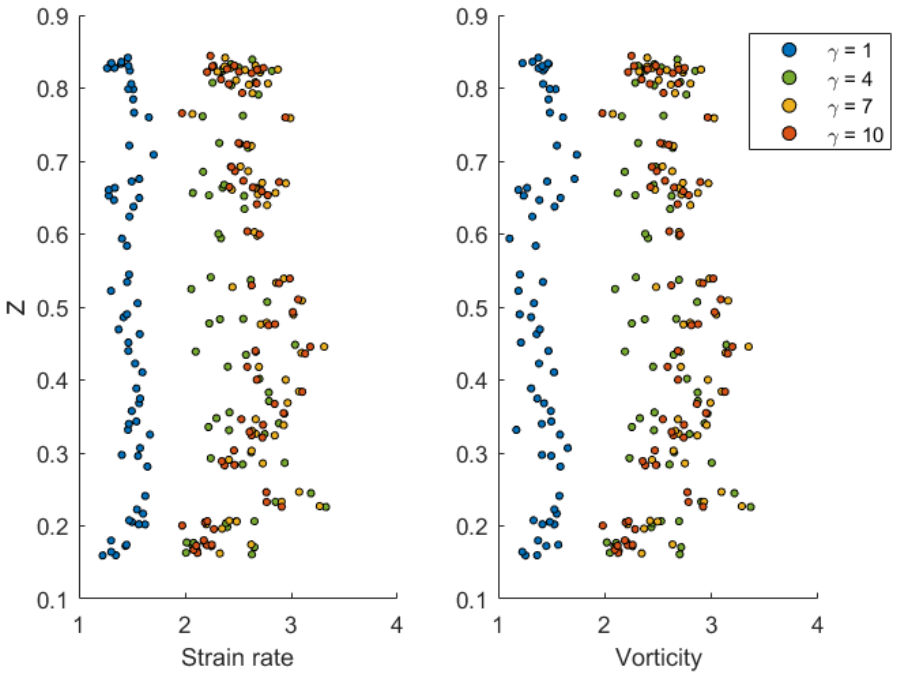

Figure 27: Mean strain rate and vorticity second invariants of each inclusion along a vertical profile. Profiles at four steps of deformation are shown. $\eta_c = 0.1$.

the centre of the model and the profile has two regions of higher values on both sides of it. On the other hand, the strain rate profile is more homogeneous from the beginning. They converge towards similar profiles already at relatively low strain ($\gamma \sim 4$, green markers) and stabilise at around $\gamma \sim 7$ (yellow markers).

Velocity.

Figure 28 shows the velocity magnitude. The white curves are streamlines, which trace the flow of material. When inclusions are the weak phase, the difference in velocity between the zones that are closer to the plates and the centre of the box is higher than in aggregates with strong inclusions. In both

cases, at the matrix-plate boundaries the streamlines are perfectly parallel to the plates, meaning that they are not being perturbed by the inclusions. However, closer to the central horizontal plane, they are affected by the presence of the inclusions and bend. If $\eta_c = 0.1$, the flow is not influenced by the inclusions until the very centre of the box, where streamlines describe ellipses (Fig. 28a). But if $\eta_c = 10$, the inclusions hinder the matrix flow more, and the majority of the volume is affected by their presence; the lines are much more perturbed too. In the centre of the model, the lines are modified by the strong inclusions. This is the place where the inclusions are less elongated and therefore the flow is more irregular. The perturbation from the imposed velocity is shown in figure 29 and it is obtained subtracting the bulk horizontal velocity from the effective horizontal velocity component v_x. The perturbation in the aggregate with weak inclusions (Fig. 29a) is more homogeneous and generally positive, which results in regular, horizontal flow lines in figure 28a. In aggregates with stronger inclusions (Fig. 29b) the perturbation is much more irregular, with positive and negative values distributed among the inclusions. This leads to more irregular streamlines, especially in regions of positive perturbation such as the centre of the cube (Fig. 28b).

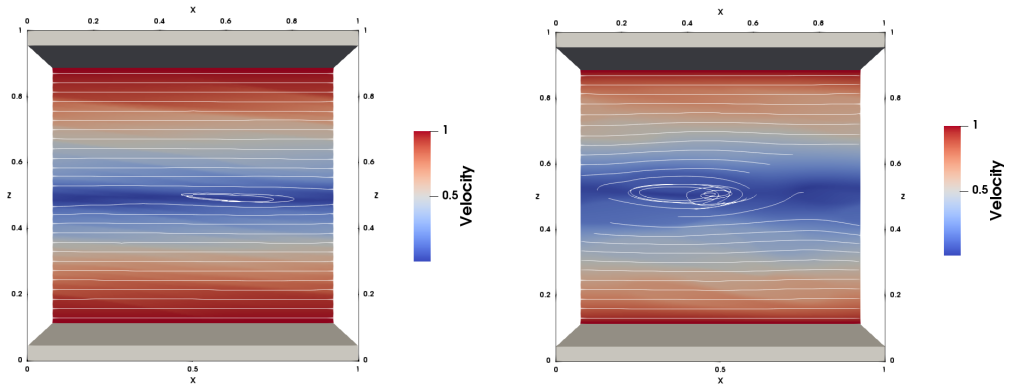

(a) $\eta_c = 0.1$ (b) $\eta_c = 10$

Figure 28: Velocity field and streamlines for inclusions 10 times weaker (a) and 10 time stronger (b) than the matrix.

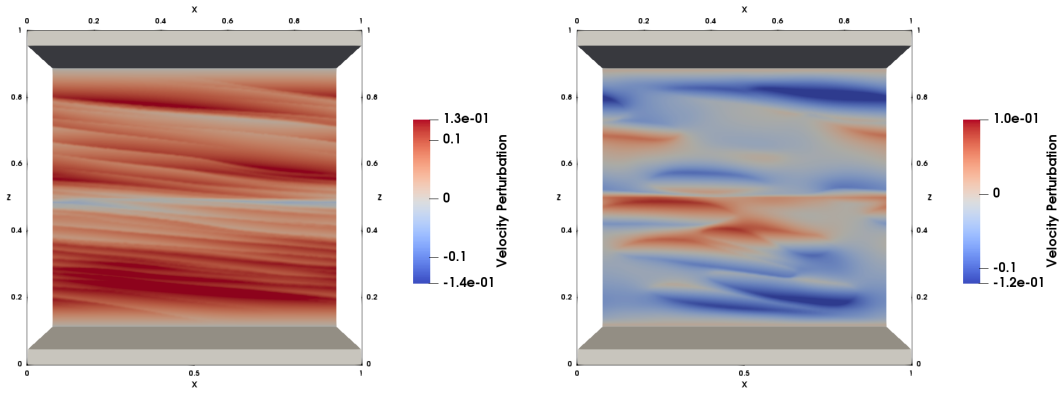

(a) $\eta_c = 0.1$ (b) $\eta_c = 10$

Figure 29: Velocity perturbation from the externally imposed velocity.

3.2 Power-law rheology

3.2.1 Fabric

As shown in the previous section, the weak phase accumulates more and more strain. Since the viscosity depends on the strain rate, the weak phase lowers its viscosity, which increases the strain rate and so on. The evolution of the fabric until $\gamma = 10$ can be found at the link in figure 30a. As reported in figure 31, the inclusions merge much more easily when they are the weaker phase, forming foliation planes which can be parallel to the boundaries (rigid plates) or 'climb' and connect to planes of a different level. These planes are where the maximum deformation localises and are found in the middle horizontal plane, symmetrical with respect to the boundaries.

The stronger phase undergoes the opposite process: as it is more viscous, it deforms much less (see animation linked in figure 30b and figure 32 at $\gamma = 10$), causing the strain rate to be very low. Consequently, the inclusion viscosity increases and their strain rate decreases. This feedback mechanism causes contrasts to be higher: variables like pressure, strain rate, stress reach more extreme values. Therefore, after the same amount of shear stress ($\gamma = 10$) the fabric that the aggregate develops shows a different structure with respect to the Newtonian case.

(a) `https://goo.gl/euHqom` (b) `https://goo.gl/EGf1pT`

Figure 30: Animation of fabric evolution in a power-law aggregate. $\eta_c = 0.1$ (a) and 10 (b).

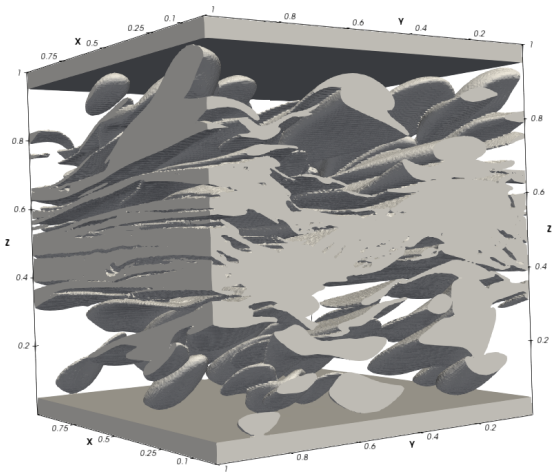

Figure 31: S-C structure developed by an aggregate with power-law rheology ($n = 3$), viscosity contrast $\eta_c = 0.1$ and volume fraction $\phi = 30$. Shear strain $\gamma = 10$.

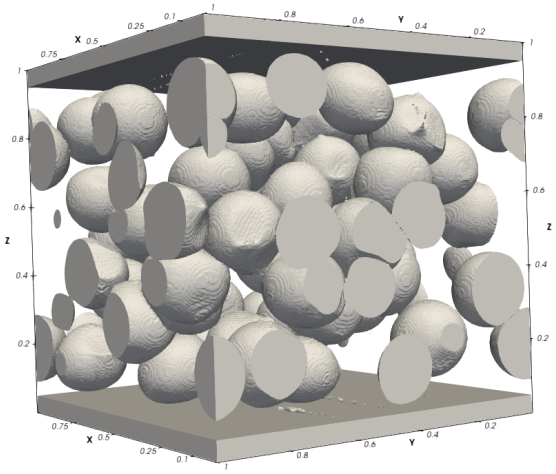

Figure 32: Aggregate with power-law rheology ($n = 3$), viscosity contrast $\eta_c = 10$ and volume fraction $\phi = 30$. Shear strain $\gamma = 10$.

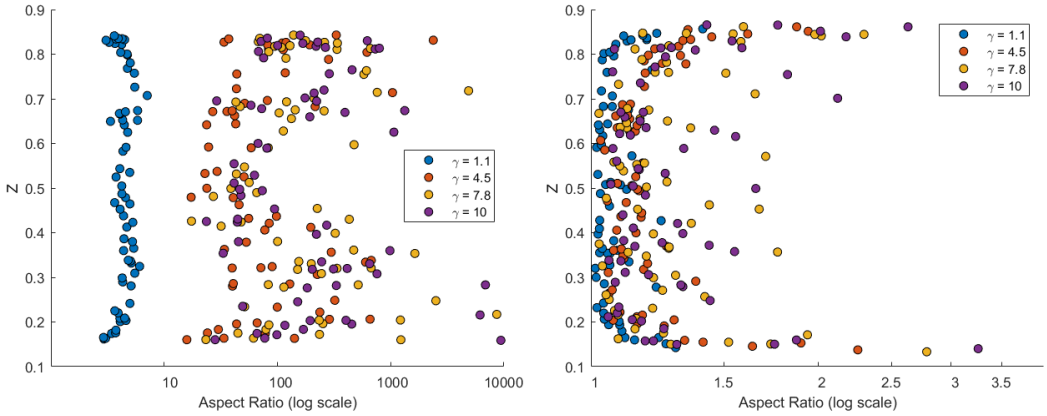

(a) $\eta_c = 0.1$ (b) $\eta_c = 10$

Figure 33: Aspect ratio of a non-Newtonian aggregate with a difference of a factor 10 between matrix and inclusions pre-exponential factor. Inclusions elongate with increasing shear strain (γ), whose increase is represented in four colours.

The difference in aspect ratio of weaker or stronger inclusions is emphasised in power-law rheology aggregates. For $\eta_c = 0.1$ in the Newtonian simulation, there is a clear trend as the inclusions elongate more homogeneously, evolving with almost the same rate. The boundary effect is more evident and their aspect ratio distribution along the vertical direction assumes a parabolic shape. With a power-law rheology, though, the aspect ratios increase much faster especially at low shear strain. The parabolic trend is less obvious (Fig. 33a). When $\eta_c > 1$, the difference with respect to the linear viscosity is greater, with only three inclusions that have an aspect ratio greater than 2 after $\gamma = 7.8$ and only one that reaches an aspect ratio > 3 (Fig. 33b). In the Newtonian rheology, all the inclusions already had an aspect ratio > 2 after $\gamma = 4.5$.

In an aggregate with power-law rheology and weaker inclusions, the strain localises in planes where inclusions merge. With randomly distributed spheres, this plane should form at the centre of the cube, symmetric with respect to

the sliding plates and the direction of shear (Fig. 34). However, if they start interconnecting at a different level, the plane that forms and accumulates the most strain might not be at the centre.

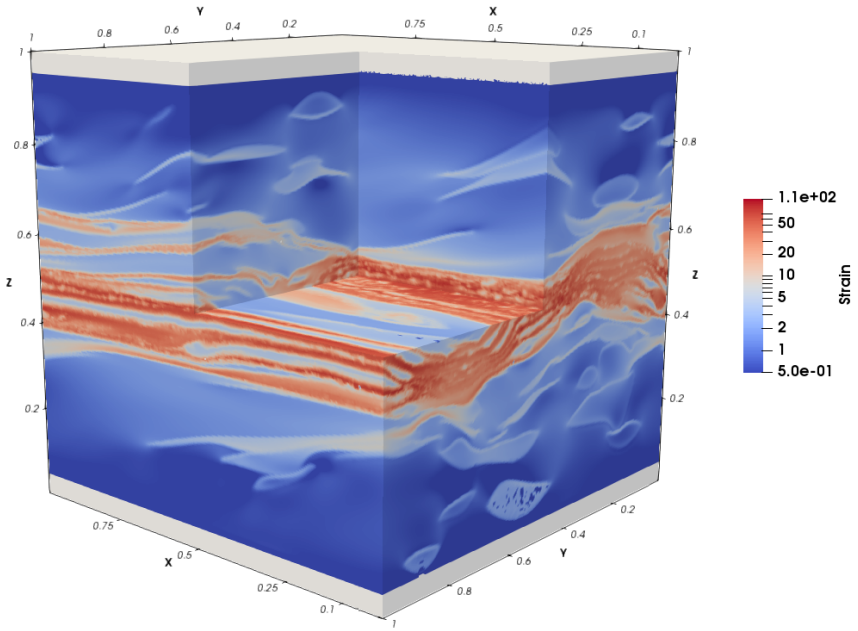

Figure 34: Strain distribution in an aggregate with weaker inclusions. $\eta_c = 0.1$, $\phi = 30\%$.

3.3 Viscosity evolution

3.3.1 Linear Rheology

We observed two types of viscosity evolution with strain, one for viscosity contrasts $\eta_c \leqslant 2$ (mode 1) and one for $\eta_c \geqslant 10$ (mode 2). All of them are included in figure 35, divided according to their mode of evolution.

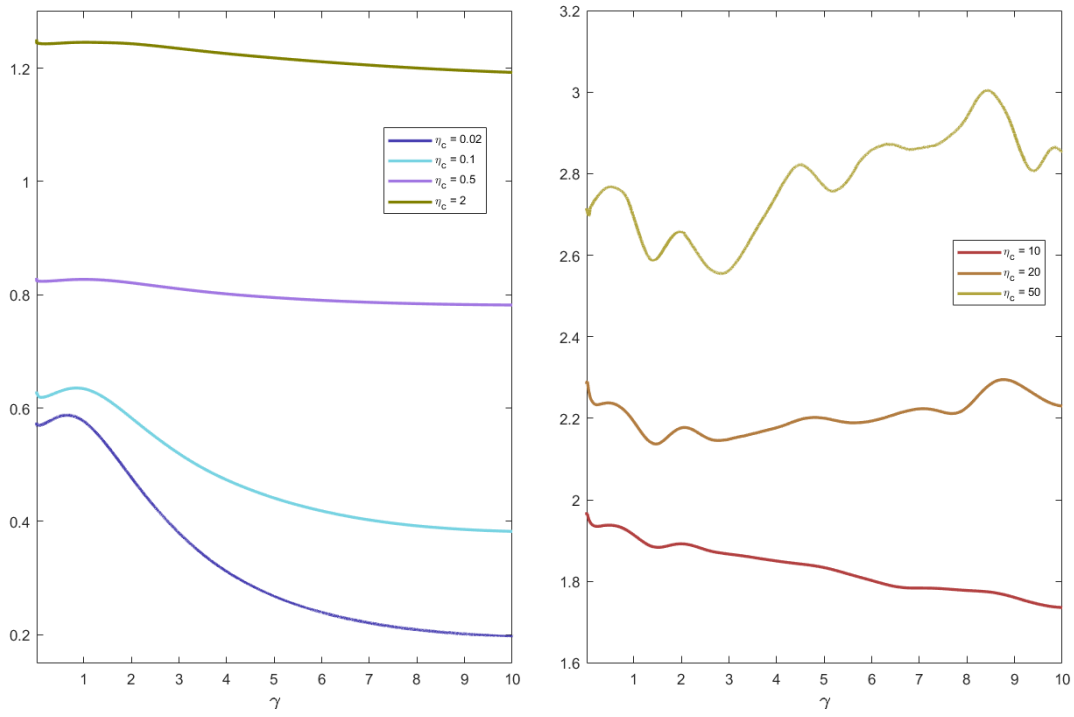

(a) Mode 1 (b) Mode 2

Figure 35: Effective shear viscosity evolution with strain for 7 viscosity contrasts. Their values are reported in the legends, the volume fraction of the inclusions is $\phi = 30$ for all of them.

Mode 1

For small values of strain, the viscosity first increases linearly with strain, but then, after reaching a maximum, it decreases exponentially towards an asymptotic value. The position of the maximum changes with different viscosity contrasts η_c (see figure 35a) and volume fractions ϕ (Fig. 36) and so does the asymptote, which corresponds to the steady-state viscosity value. In this case, the effective shear viscosity decreases as strain is applied and as the inclusions flatten. A great decrease in viscosity happens when inclusions merge, creating planes of weakness where the deformation can localise.

We include aggregates with stronger inclusions but low viscosity contrasts in this mode because the aggregate's effective viscosity trend resembles the ones that weaker inclusions form. We do not observe dramatic decreases in bulk viscosity when the merging is not very efficient ($\eta_c = 0.5$ or $\eta_c = 2$).

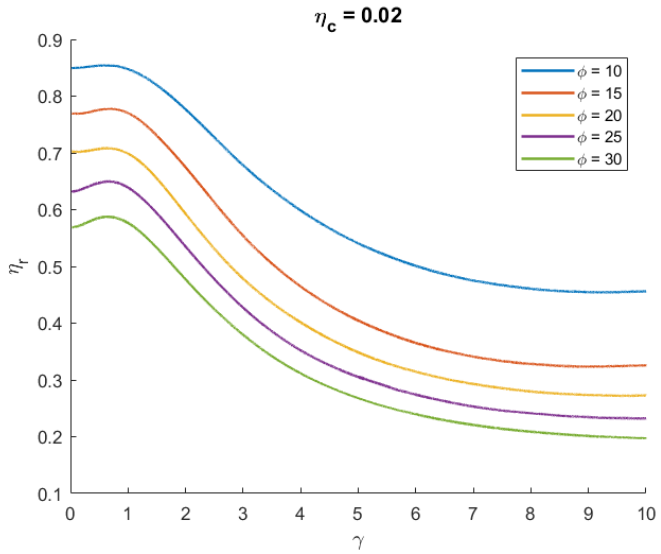

Figure 36: Mode 1 evolution with strain of bulk effective shear viscosity normalised to the matrix viscosity. Inclusions are weaker than the matrix ($\eta_c = 0.02$) in all the curves, volume fractions $\phi = 10\%, 15\%, 20\%, 25\%, 30\%$.

Mode 2

Mode 2 includes viscosity trends that don't reach a steady-state value before $\gamma = 10$ and is reported in figure 37. They keep oscillating as the strain increases, though a decrease of the amplitude of such oscillations is observed in some cases (e.g. $\eta_c = 10$).

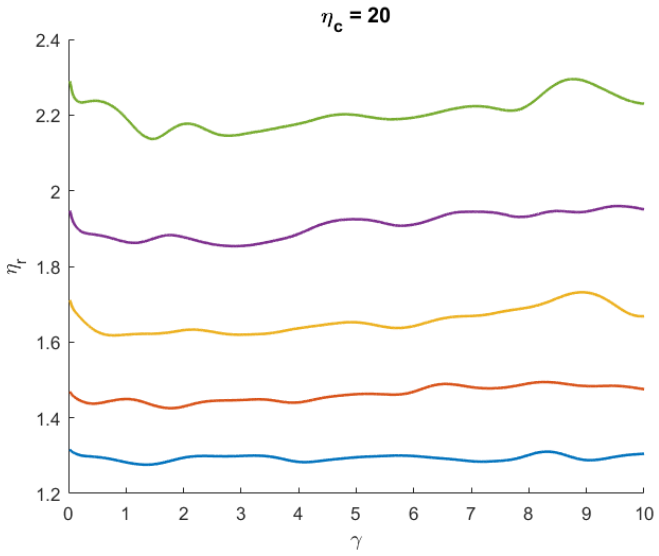

Figure 37: Mode 2 evolution with strain of bulk effective shear viscosity normalised to the matrix viscosity. Inclusions are stronger than the matrix ($\eta_c = 20$) in all the curves, volume fractions $\phi = 10\%, 15\%, 20\%, 25\%, 30\%$. See figure 36 for the legend.

As reporting the effective shear viscosity as a function of three parameters would require four dimensions, all the effective viscosity evolutions are reported in figure 38 as functions of η_c and γ on three planes representing three different volume fractions. Values of η_r for $\eta_c < 1$ have been plotted as $-1/\eta_r$ to emphasise the difference in η_r.

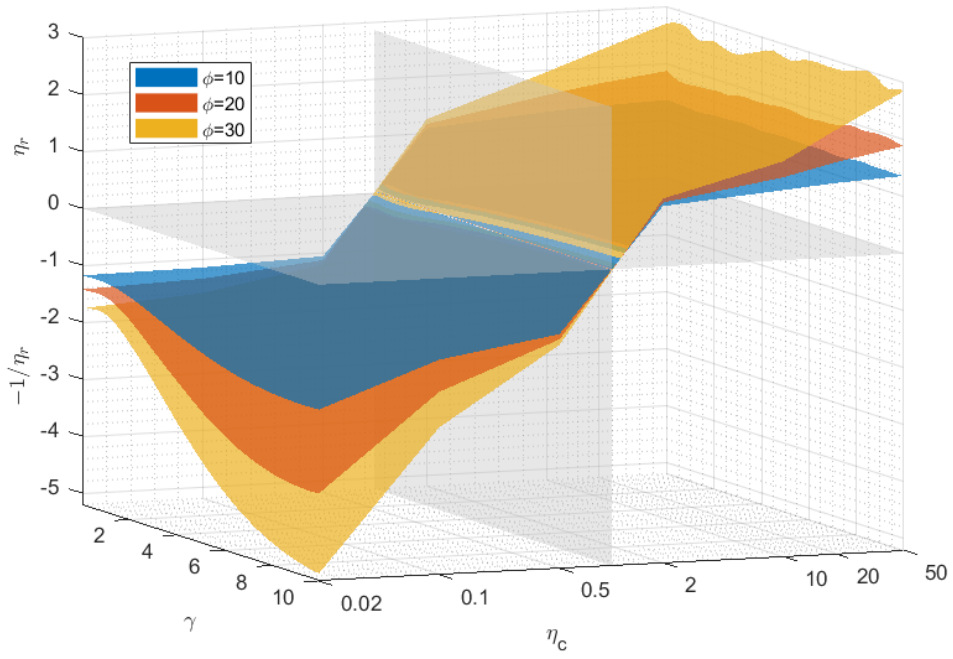

Figure 38: Effective shear viscosity of all simulations with $\eta_c = 0.02, 0.1, 0.5, 2, 10, 20, 50$ and $\phi = 10\%, 20\%, 30\%$. Surfaces between actual values are interpolated. Vertical and horizontal planes are at $\eta_c = 1$ and $\eta_r = 0$ for reference.

3.3.2 Power-law rheology

The effective shear viscosity evolution of an aggregate with a weak phase immersed in a stronger matrix is reported in figure 39a. The effective viscosity of a Newtonian aggregate is added for comparison. For $\eta_c = 0.1$, the trend is the same as the one of a Newtonian aggregate, after an initial growth in the effective viscosity, it reaches a peak and decreases towards a plateau at higher shear strain values. However, the difference in viscosity between the two rheologies increases with increasing strain. While in the Newtonian case the effective viscosity decreases by two thirds, the viscosity of the non-Newtonian one halves.

The trend in the case of a non-Newtonian rheology, however, is much more different from the one of a Newtonian rheology when inclusions are stronger than the matrix. For $\eta_c = 10$ and a Newtonian regime, there are some oscillations in the bulk viscosity values, but overall it decreases as the system stabilises. But with a power-law rheology, the inclusions are too strong to find an stable configuration and keep blocking the flow, increasing the bulk viscosity value more and more (Fig. 39a).

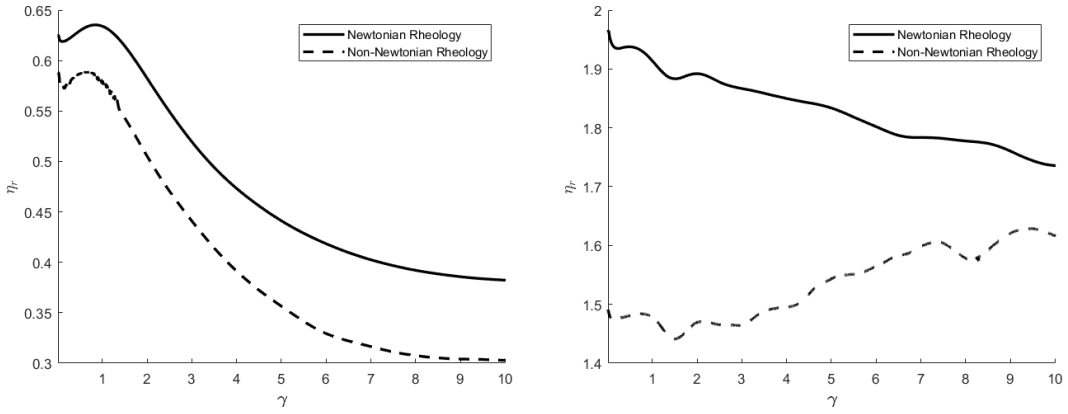

(a) $\eta_c = 0.1$ (b) $\eta_c = 10$

Figure 39: Comparison between bulk viscosities of an aggregate with Newtonian (solid line) and power-law rheology (dashed line). The first one has a viscosity contrast $\eta_c = 10$, in the second, 10 is the contrast in pre-exponential factor of inclusions and matrix. The volume fraction of the second phase is 30 for both aggregates.

3.4 Viscosity Parametrisation

We wanted to find an equation that predicts the effective shear viscosity of the aggregate evolution with strain and as a function of viscosity contrast and the volume fraction of the second phase. In order to obtain such an equation, we plotted the viscosity curves for every combination of viscosity contrast and volume fraction that we simulated and fit a curve to them. The fitting process was done in MATLAB with a function that uses least squares regression to minimise the residuals of the points from the curve. Viscosity contrasts η_c less than 10 show a behaviour similar to each other that can be described by a general equation with only a few changing parameters.

In a Newtonian regime, their curves have a similar trend and the equation that best predicts the data is:

$$\eta_r(\gamma, \phi, \eta_c) = c_1(\gamma + c_2)e^{-\gamma/c_3} + c_4 \tag{19}$$

where the coefficients c_i are a function of the viscosity contrast η_c and of the volume fraction ϕ. In particular, c_4 is the value of the relative effective viscosity (η_f) when the aggregate has reached a steady-state condition, $\eta_r(\gamma \to \infty)$.

Equation 19 describes a curve that initially increases, reaches a maximum and then exponentially decreases towards an asymptotic value. The first growth in effective bulk viscosity is described by a linear dependence of η_r on γ. The slope and the γ interval in which this behaviour is observed depend on the viscosity contrast η_c and on the volume fraction ϕ. In particular, the slope when $\gamma = 0$ is the first derivative of equation 19:

$$\frac{d\eta_r}{d\gamma} = c_1 e^{-\gamma/c_3}\left(1 - \frac{\gamma + c_2}{c_3}\right) \tag{20}$$

when $\gamma = 0$:

$$\frac{d\eta_r}{d\gamma}(\gamma = 0) = c_1 \left(1 - \frac{c_2}{c_3}\right). \tag{21}$$

The first derivative is positive before the maximum, which is reached when it becomes zero, more precisely at:

$$\gamma_m = c_3 - c_2 \tag{22}$$

The curve then decreases towards the asymptote with a negative exponential trend. The steepness, and therefore the speed with which the final value is reached, depend on the third coefficient, c_3.

The steady-state η_r final value is c_4: when $\gamma \to \infty$, the exponential tends to zero and the only coefficient left is c_4.

All of these coefficients are functions of η_c and ϕ, and once they have been set, they contribute to build the equation for the bulk effective viscosity. Their role in the equation is discussed in the following paragraphs. The volume fraction of the inclusions is expressed as a fraction of 1.

First coefficient, $\mathbf{c_1}$

The role of c_1 in the curve is not straightforward. It is however one of the main components of the initial slope (equation 21). Its expression is:

$$c_1 = 0.0668 \,|\log \eta_c\,|^{7/5} \tag{23}$$

The fitting has an $R^2 = 0.951$.

c_1 is a function of the natural logarithm of η_c, therefore $c_1 = 0$ when $\eta_c = 1$, meaning that the slope is zero if there is no viscosity contrast. In fact, if the material is homogeneous, the graph for the viscosity is expected to be an horizontal line at $\eta_r = 1$ (first derivative = 0). c_1 becomes greater farther from

the central value of 1 along the η_c axis in both directions. This is an effect of applying the absolute value to the logarithm. The surface is not as sharp as the magnitude of a logarithmic function would be, because the exponent 7/5 smooths the function around $\eta_c = 1$. For $\eta_c \to 0$, which corresponds to high viscosity contrasts when the inclusions are weaker, c_1 increases. This is consistent with the observations made in section 3.3: stronger viscosity contrasts lead to marked initial increases in effective viscosity. The coefficient c_1 and the volume fraction ϕ don't have a clear correlation, so we considered the coefficient to be independent of ϕ. Its curve is reported in figure 40 with a surface together with the values of c_1 obtained from the fitting of equation 19. It describes the c_1 values with $R^2 = 0.951$.

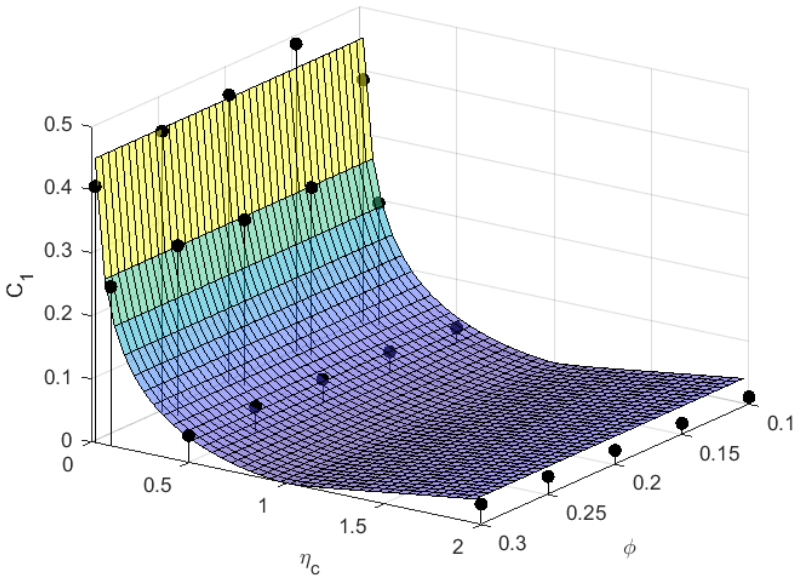

Figure 40: Parametrisation of the first coefficient as a function of η_c and ϕ. The black points are the coefficients c_1 for all the Newtonian simulations found with the fitting of equation 19.

Second coefficient, c_2

The second coefficient has influence on the position of the peak value of the effective viscosity along the γ axis and on the initial slope. As described by equation 22, the maximum position on γ is a function of c_2 and c_3. For small values of c_2, the peak value moves towards higher values of γ and vice versa.

Its expression is:

$$c_2 = 0.224\,\eta_c^2 - 0.0137\,\eta_c + 0.872 \tag{24}$$

which is a second degree polynomial in η_c. It is almost constant with ϕ, with a few exceptions that cannot be taken into account when modelling c_2 as a function of the two parameters at a time. Equation 24 is plotted in figure 41, the fitting has an R^2 of 0.974.

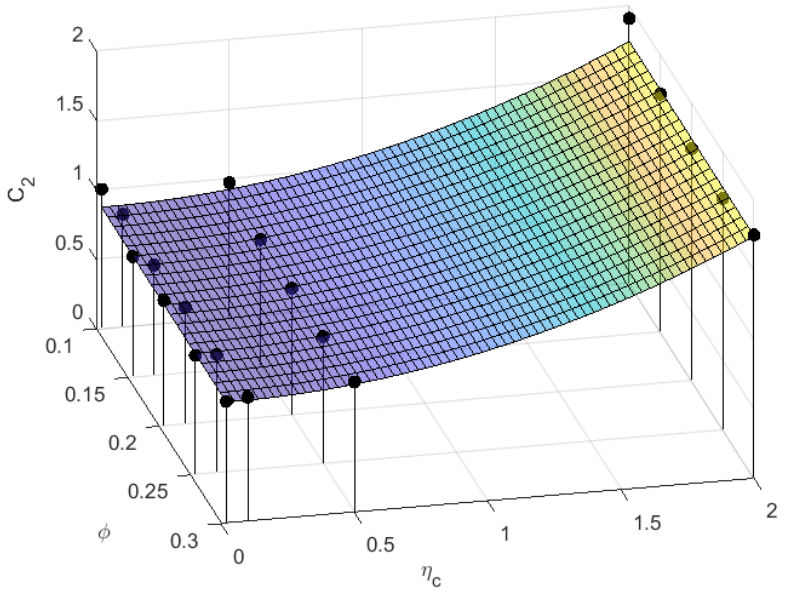

Figure 41: c_2 as a function of η_c and ϕ.

Third coefficient, c_3

c_3 is the coefficient that divides γ at the exponent. The exponent is negative and causes the viscosity to decrease. The value of c_3, for a fixed value of ϕ, linearly increases with η_c (see figure 42), causing the exponential curve to decrease more gently, as it is divided by a greater value. It also appears in the equation for the position of the peak value along the γ axis (equation 22). It results that the greater c_3 is, the more the peak value moves towards higher values of γ.

The expression for c_3 is:

$$c_3 = 0.6317\,\eta_c - 0.1039\,\phi + 1.4415 \tag{25}$$

This coefficient is linear in both η_c and ϕ. Except for an anomaly for $\eta_c = 0.02$ and $\phi = 0.1$, the model reproduces the coefficient values well. R^2 is 0.987, the curve described by equation 25 and values of c_3 are reported in figure 42.

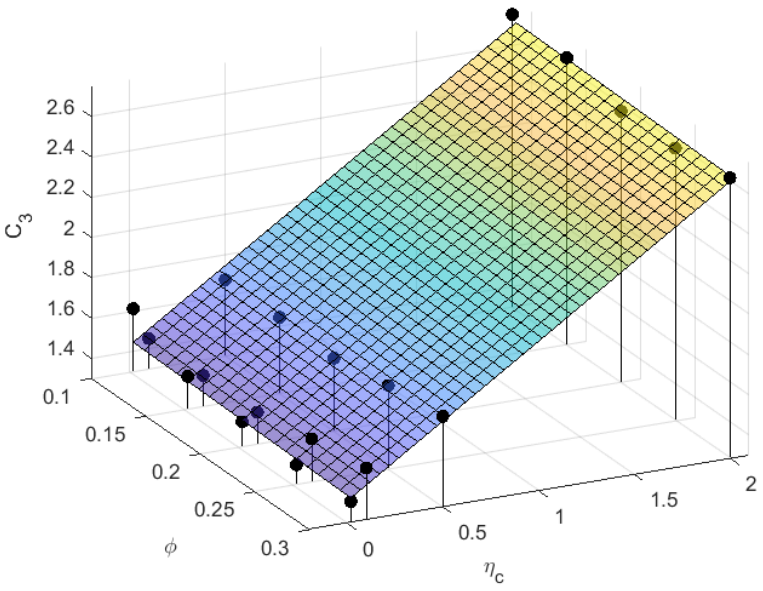

Figure 42: Fitting of c_3 as a function of η_c and ϕ.

Fourth coefficient, $\mathbf{c_4}$ or η_f

The fourth coefficient is probably the most important of all coefficients, as it represents the final value of η_c, that is the effective bulk viscosity that the aggregate reaches steady state conditions, η_f. It is the value towards which the viscosity curve tends when $\gamma \to \infty$.

$$\eta_f = c_4 = 0.8209\,(\log \eta_c)\,\phi + 1 \tag{26}$$

where $\log \eta_c$ denotes the natural logarithm. When $\eta_c < 1$, c_4 decreases with ϕ, because $\log \eta_c < 0$. This is a reasonable behaviour, since higher volume fractions of a weak material decrease the aggregate bulk viscosity. Conversely, when $\eta_c > 1$, $\log \eta_c > 0$ and the bulk viscosity becomes greater with the increase of the volume fraction of the stronger phase. When $\eta_c = 1$, which means that there is no viscosity contrast, $\log \eta_c = 0$ and $\eta_f = 1$. The curve is displayed in figure 43, $R^2 = 0.982$.

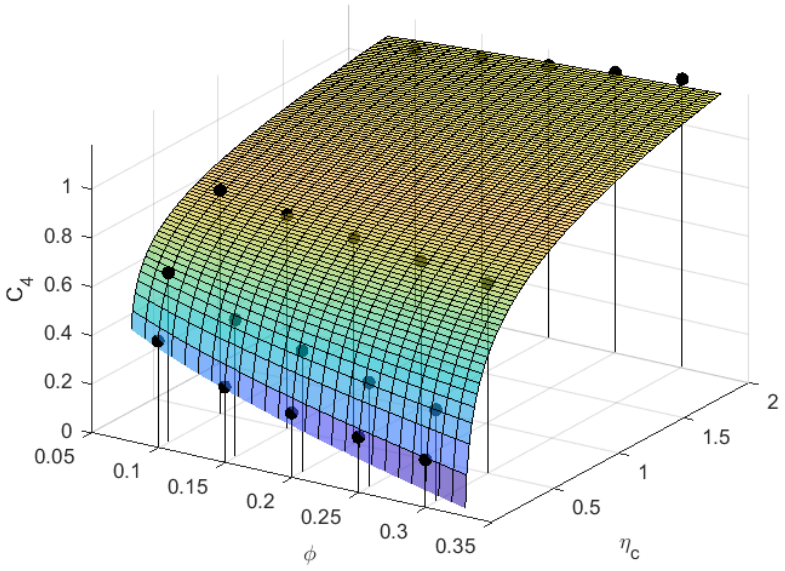

Figure 43: c_4 and steady-state value of η_r as a function of η_c and ϕ.

When combining all these coefficients into the general equation of η_r evolving with γ (equation 19), we observe that is easier to model higher viscosity contrasts (e.g. η_c=0.02 or 0.1) with respect to aggregates in which the difference in viscosity is lower (Fig. 44). This is due to the clearer shape that curves of higher contrast aggregates assume, when the trend is more pronounced: sharp increase, peak value and exponential decrease. Lower contrasts produce smoother curves, in which the coefficient roles are less clear and more difficult to identify. Their curves vary little with γ, therefore errors that are small in absolute value become much bigger when applied to curves that do not vary much.

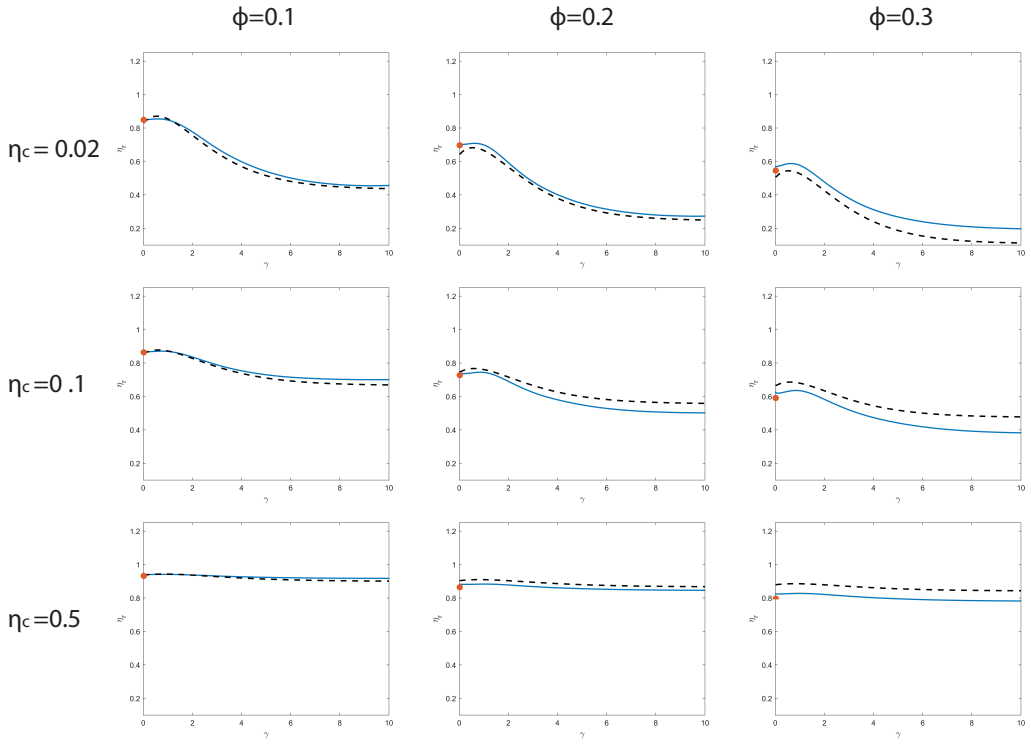

Figure 44: Effective shear viscosities of aggregates with different viscosity contrasts and volume fractions. Solid lines are the results of the numerical simulations. Dashed lines are the model calculated with equation 19 where the coefficients c_i have been computed with equations 23, 24, 25 and 26. The red point is the predicted initial value of bulk effective viscosity calculated with equation 27.

Smaller values of ϕ are easier to model, this might be because high values involve more sphere interactions, which are less predictable.

Initial value, η_{r_0}

We modelled the effective shear viscosity of the incipient stage. The data of η_r are taken at $\gamma = 0.02$.

The equation that best fits the values is:

$$\eta_{r_0} = \left(1.1684\,(\eta_c - 1) - 0.33109(\eta_c - 1)^2\right)\,\phi + 1 \tag{27}$$

which is the second-degree Taylor polynomial approximation at the point $\eta_c = 1$ and it is plotted together with the data of the initial value in figure 45. For constant values of ϕ, the η_c-η_{r_0} relationship is almost linear, but it can be better approximated by a Taylor polynomial.

Keeping η_c constant, the value of η_{r_0} decreases as ϕ increases when $\eta_c < 1$. In fact, when $\eta_c < 1$, $\eta_c - 1 < 0$ and ϕ decreases. It means that the greater volume of weaker inclusions there is, the smaller the bulk viscosity will be. When $\eta_c > 1$, we observe the opposite situation: a greater volume (increase in ϕ) causes an increase in the effective bulk viscosity. The equation and actual values of η_{r_0} are plotted in figure 45, $R^2 = 0.995$.

Initial values of viscosity were also compared with the analytical solution by Hsueh & Wei (2009) for effective viscosity of suspensions of monosized hard spheres (eq. 3). In this case, we considered only initial values before our spheres start to deform, because Hsueh and Wei's equation is only valid for spherical inclusions. This comparison is reported in figure 46.

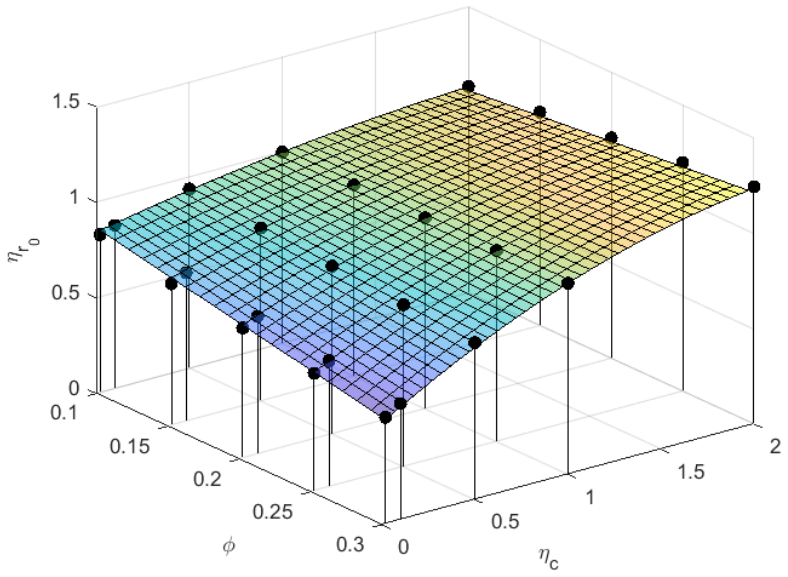

Figure 45: Initial effective bulk viscosity values as functions of η_c and ϕ.

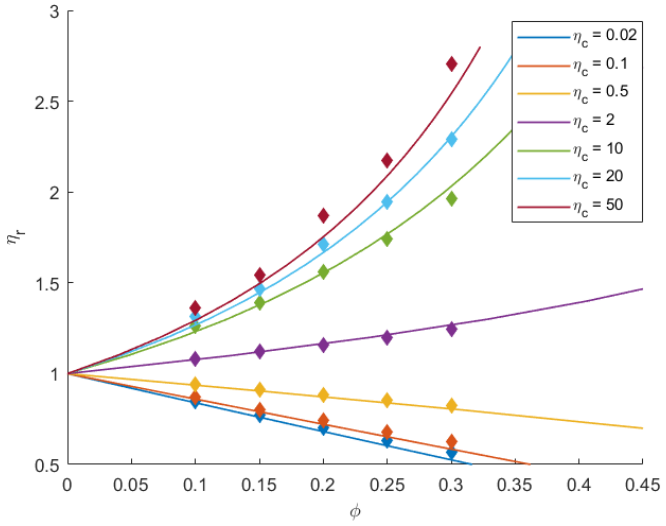

Figure 46: Values of relative effective viscosity η_r predicted by Hsueh & Wei (2009) with an analytical solution for monodispersed suspensions of hard spheres (solid lines) and results from our numerical simulations, initial values for $\gamma = 0.0222$.

4 Discussion

4.1 Viscosity and fabric

Strong inclusions. The oscillatory trend of the bulk effective shear viscosity for aggregates with strong inclusions is interpreted as a consequence of the inclusion position. In fact, for $\eta_c \geqslant 10$ and in particular for $\eta_c \geqslant 20$, the inclusions oscillate along the z (vertical) direction because of the interaction with other particles (Fig. 18). When an inclusion that is moving horizontally because of the imposed shearing finds another inclusion along its trajectory, it is pushed in the vertical direction away from the central flow. The other inclusion is consequently pushed in the opposite direction. Many of these processes happen during the deformation and these multiple interactions are reflected in the effective bulk viscosity (e.g. Fig. 37). The effect is intensified by the confinement of the two rigid plates. Since the shear zone thickness is limited by the presence of two non-deformable and unmovable plates, the inclusions are not allowed to move away from each other, which forces more interactions between them.

This effect is particularly evident at the beginning of the deformation process. In fact, the inclusions are still spherical (i.e. they haven't started elongating yet), which causes them to be more likely to interact with each other and so their trajectory depends much more on the geometrical distribution of the particles. If two inclusions are close to each other, they are bound to modify their trajectories because of the presence of the other one and their vertical position is the consequence of the position of other particles. In this phase, the tiling-up process plays a fundamental role in the microstructure and consequently in the viscosity evolution.

Oscillations in the effective bulk viscosity are amplified by high viscosity

contrasts. When the contrast is greater than 10, the inclusions are too strong to develop an elongated shape that would allow the flow to be parallel to the boundaries before $\gamma = 10$ (see $\eta_c = 20$ or $\eta_c = 50$ in figure 35). Their effective bulk viscosities keep fluctuating and the general trend is positive, with oscillations that depend on the interactions. We expect this trend to invert when the inclusions will start to deform more efficiently and the structure will allow a less disturbed flow, but this could require much higher strains.

Sudden increases of effective shear viscosity correspond to situations in which the particles entangle themselves in cluster of strong particles blocking the flow. Larger inclusions enhance the clustering process as they are more likely to tile up. This configuration makes the viscosity unpredictable, since it strongly depends on the initial distribution of inclusions and the greater the contrast is, the more complicated the curve becomes. In the end-member case in which the particles are rigid and non-deformable, they will keep interacting with each other without finding a stable configuration.

For $\eta_c = 10$, the combination of tiling-up and inclusion elongation makes the viscosity curve decrease with some fluctuations, meaning that the strength of the inclusions causes them to interact and hinder the flux, but, especially at greater strains, their elongation reduces the interactions and leads to a more stable configuration.

This does not happen in the case of a power-law regime for the same η_c. The particles are too strong to deform and they will preserve a nearly spherical shape even if the applied shear strain is very high. The inclusions cannot reach a stable configuration and the flow is continuously deviated by the presence of these obstacles. The general trend is more similar to the ones with higher contrasts in the Newtonian regime. The inclusions keep forming blocks for the material flow and this behaviour is still observed when the contrast is 5 in the

power-law viscosity.

In summary, the main factors that lead to greater oscillations in the viscosity trend are a greater viscosity contrast, a higher volume fraction of the strong inclusions, their greater size, the confinement of the shear zone and the (spherical) shape of the inclusions, which is a function of the shear strain. Oscillations and increases in viscosity are emphasised in the case of non-Newtonian rheology.

Weak inclusions. The initial increase in effective viscosity observed in aggregates with weaker inclusions (Fig. 36) is interpreted to be caused by the inclusion behaviour when they are still nearly undeformed. In fact, they are passive elements in the matrix flow and, before they interconnect, act like stronger inclusions do, tiling up and increasing the viscosity. The load-bearing framework is the matrix, as it is the only phase that accommodates stress at the beginning of the deformation. The inclusions push against each other and hinder the flow, strengthening the aggregate. The higher the viscosity contrast (i.e. the lower the viscosity of the weak phase), the stronger this effect is. This is due to the fact that, at high viscosity contrasts, we observe a stress concentration in the matrix: the stress partitioning between the two phases is more extreme (see figure 23). Once the highest value of viscosity is reached, the inclusions start accommodating strain and only at this point the viscosity decreases. The value of strain at which the maximum is reached does not seem to depend much on the volume fraction of the weak phase (Fig. 36), but rather on the viscosity contrast (Fig. 35a).

Another important step in the effective bulk viscosity evolution is when the percentage of strain accommodated by the inclusions becomes greater than the fraction of strain accommodated by the matrix. For example, this is found at $\gamma \sim 2.2$ for $\eta_c = 0.1$ and $\phi = 30$ (minute 0:08 of the animation at the

link in figure 12a). It happens when, after some more application of strain, the matrix, although difficult to deform, allows the inclusions to interconnect. This efficient deformation stops the tiling-up and leads to the formation of very elongated and flat interconnected inclusions that allow a nearly laminar flow (Fig. 28a).

For very low viscosity contrasts, which are when the inclusions have a viscosity that is twice or half the viscosity of the matrix, the stable configuration is reached at very low strains ($\eta_c = 0.5$ and $\eta_c = 2$ in figure 35a). This is caused by the fact that the aggregate deforms in an almost homogeneous way: the difference in behaviour between the strong and the weak phase is very small. The inclusions interact very little and only at the beginning of the strain application, which causes the viscosity to increase like in the previously described case, although the increment is much smaller. The aggregate soon reaches a stable condition when they start to elongate in parallel to the flow direction (Fig. 14). Due to the similar behaviour between inclusions and matrix, having stronger or weaker inclusions does not make a big difference in the viscosity evolution, as long as the contrast is low.

Our results are in accordance with Girard et al. (2016), who observed that at large strain the rheology of the aggregate is controlled by the weaker phase.

Wang et al. (2013) observed instead strain hardening for strain less than 20% in their CaGeO3 perovskite (GePv) - MgO aggregate, which is consistent with the experimental results by Girard et al. (2016) and with our numerical experiments at these low strains.

The numerical study by Madi et al. (2005) on a bridgmanite and ferropericlase mixture showed little strain partitioning, although they considered very small strain ($\sim 10^{-4}$). They don't calculate the effective bulk viscosity.

4.2 Viscosity Parametrisation

As reported in section 3.4, to describe the bulk effective shear viscosity evolution, our simulations have been split into two sets. The first one includes aggregates with inclusions less viscous than the matrix ($\eta_c < 1$) and inclusions more viscous, but with low viscosity contrasts ($\eta_c \leqslant 2$, mode 1 in figure 35a). This division considered the fact that inclusions 5 times stronger than the matrix and more (mode 2, figure 35b) don't reach a stable configuration soon enough to be predicted by a (simple) equation. This is caused by the fact that their strong viscosity contrasts do not let the inclusions deform enough to allow a smooth flow. Therefore, the effective viscosity oscillations depend on how much the inclusions interact with each other, which is determined by their initial distribution much more than other parameters.

Mode 1 evolution has been fitted with equation 19 and the equations that follow it for the coefficients c_i. The evolution of η_r with γ has the same shape described by equation 19, while η_c and ϕ influence the initial and final (steady-state) values, the initial slope, the position and height of the peak value and the slope of the exponential decrease.

The viscosity contrast, η_c, is the parameter that makes the curve change the most. Every c_i coefficient is a function of it and many of them depend on it in a way that is stronger than linear (e.g. quadratic, equation 24). In particular, η_c has a great influence on the initial positive slope, which is higher when the viscosity contrast is larger, as discussed in section 4.1.

It also has an important role on the slope of the exponential decrease, which is related to how fast the aggregate reaches a steady state. The greater the viscosity contrast for weak inclusions ($\eta_c << 1$) is, the faster the exponential decrease becomes. This implies that at high viscosity contrasts, the difference between the initial and the final (steady-state) values is much greater (e.g.

$\eta_c = 0.02$ in figure 35a).

The fact that η_c influences these two values is evident. There is a positive correlation between the viscosity contrast and the effective shear viscosity at $\gamma = 0$, approximated with a second-degree Taylor polynomial (equation 27), whereas the relationship between η_c and the steady-state value is observed to be logarithmic (equation 26).

Logarithmic relationships are common between η_c and other parameters or coefficients, as the change in sign at $\eta_c = 1$ can describe a different behaviour of contrasts that are < 1 and > 1.

The volume fraction has also an important role on the initial and steady-state value, making the viscosity of the weaker phase less or more important in the bulk one. On the other hand, its role seems less straightforward in other parameters such as the peak value position on the γ axis or the steepness of the exponential.

4.3 Aspect ratio and deformation distribution

When inclusions are weaker than the matrix and especially in a non-Newtonian regime, the inclusion position is crucial to the resulting microstructure and, consequently, to the effective viscosity. In fact, due to the initial random distribution, it is possible that two inclusions are relatively close to each other. If they are in this particular configuration, they are much more likely to interconnect. This leads to a very efficient strain localisation in the flat interconnected inclusions. In our first numerical experiment with a random distribution of spheres that have all the same dimension, we observed a peak in the strain localisation, that was reflected in the aspect ratio distribution too (Fig. 33a), in a non-symmetrical distribution with respect to the plates (e.g. in the animation linked in figure 30a). This asymmetry can only be explained with this

geometrical factor. In fact, with a different initial distribution (i.e. polydispersed), the position of the localisation plane changes (Fig. 31).

The effect of boundary localisation is observed in every simulation and it is very clear in all of them. For $\eta_c < 1$, the matrix is the load-bearing framework at the beginning, forming more rigid layers close to the matrix, therefore the more deformable portion is the central one, where the weak inclusions are concentrated. In this configuration in which the boundaries are stronger, the aspect ratio shows higher values at the centre of the model (Fig. 33a). This situation persists until medium values of γ ($\gamma \sim 3.5$ for $\eta_c = 0.1$ and $\phi = 30$), when the concavity of the aspect ratio profile along the vertical axis changes. This means that boundary localisation only happens over a threshold value of shear strain. Once the threshold has been passed, the mechanism is very efficient, leading to differences in aspect ratio between boundaries and center of two orders of magnitude.

In a power-low regime we were expecting this trend to be emphasised. However, the values of maximum aspect ratio have the same order of magnitude and the boundary localisation is more efficient in the case of linear viscosity than in non-Newtonian rheologies (Fig. 33a). This is interpreted to be the effect of two opposite mechanisms of localisation: the first one, boundary localisation, concentrates the deformation at the boundaries and is more active at low strains; the second one is the efficient localisation caused by the interconnection of the inclusions that form planes of weakness in which aspect ratio increases consequently. The first mechanism acts closer to the plates, increasing the inclusion aspect ratio at the boundaries, the second one causes the aspect ratio to be greater at the centre of the model, or, more generally, along the plane of strain localisation. Therefore, the aspect ratio distribution is not as clear as in the Newtonian aggregate, but appears more scattered due to the combination of the two effects.

In aggregates with strong inclusions, although the distribution of aspect ratio along the vertical direction shows the same concave shape, the difference in values is much smaller (Fig. 33b). The layer of matrix situated between the plates and the volume of matrix and inclusions is now the weaker phase, which causes the localisation to start immediately. In fact, the elongation at the boundaries already starts at low strains.

In this case, having no localisation on central planes and the only places of localisation being the boundary zones, the concavity is more evident in the non-Newtonian regime, especially at intermediate strains. The central particles are almost non-deformed while ellipticity of the inclusions at the boundaries is two or three times greater. The over-all deformation is very low and the elongation occurs only at the boundaries.

Boundary localisation is observed in nature: A rock containing a layer with a different viscosity, like dykes or veins, sharply concentrate shearing at the boundary if the layer is stronger than the host rock. Having homogeneous composition and structure, the strain is accommodate homogeneously throughout the layer (Pennacchioni & Mancktelow, 2007).

5 Conclusions

In this thesis, we have studied how the viscosity contrast and the volume fraction of a second phase affect the microstructure of a two-phase aggregate deformed by simple shear. The bulk effective shear viscosity is a consequence of the microstructure, which means that it depends on the two aforementioned parameters and evolves with strain. To study their influence on the fabric and the bulk viscosity, we performed 3-D mechanical simulations on two-phases crystalline aggregates, both in Newtonian and non-Newtonian regimes and up to shear strain of 10.

Based on the parameters we considered, we can conclude that the microstructure and bulk effective shear viscosity are affected by:

- viscosity contrast (η_c): It is the most important amongst the studied parameters, as the presence of a second phase with different viscosity influences the bulk viscosity from the beginning and determines the different behaviour of the inclusions with respect to the matrix. It is the parameter that determines whether the inclusions elongate and assume the form of a prolate ellipsoid ($\eta_c > 1$) or flatten out as oblate ellipsoids ($\eta_c < 1$). It controls the partitioning between the two phases of variables such as pressure, strain, strain rate, vorticity, velocity.
- volume fraction (ϕ): It is a crucial parameter because it directly affects the bulk viscosity, but it also determines how the inclusions are interacting with one another. More inclusions result in more interaction: in the case of strong inclusions, this causes more repulsive interactions and unstable situations; whereas having more weak inclusions makes them more likely to merge.
- viscosity regime: It directly affects the matrix and inclusions viscosity, which remain constant in the case of Newtonian simulations, whereas

they depend on the strain rate distribution in the non-Newtonian regime. Therefore, it has a fundamental role in the microstructure and viscosity evolution, as it emphasises the contrast in viscosity and makes strong inclusions more viscous and weak inclusions less viscous.

- initial distribution of the inclusions: The microstructure also depends on the initial distribution of the inclusions. In the case of weak particles, it controls where the foliations planes are more likely to develop; in the case of strong inclusions, it determines how the inclusions are interacting with each other. Nevertheless, the effect on the bulk viscosity is minor.
- size and shape of the inclusions: in a polydispersed suspension, inclusions manage to interconnect more easily than in a monodispersed one. However, the effect is much less evident with respect to the previous parameters and the difference in viscosity is almost negligible.

In addition to a qualitative description of the influence of the viscosity contrast and volume fraction, we derived an equation from the numerical simulations for the bulk effective shear viscosity as a function of the two parameters and the shear strain for linear rheologies. It consists of an initial linear growth of the viscosity with the shear strain, followed by an exponential decrease towards an asymptotic value (steady-state condition). The slope of the curve, its initial and steady-state values are functions of η_c and ϕ.

5.1 Future Research

The current version of the code considers intercrystalline dynamics, solving the the fundamental equations of the continuum mechanics. However, real minerals can alter their structure as a consequence of strain application via intracrystalline deformation.

Therefore, more processes could be taken into account, like pressure-solution, or intracrystalline processes like CPO evolution, dynamic recrystalisation. They weren't implemented in this version of the code, but they would help reproducing more accurately what happens in natural rocks.

We only studied non-Newtonian rheologies with the power law exponent $n = 3$, but in future studies, different exponents could be investigated.

As for the localisation at the boundaries, further numerical simulations with different initial distribution of the inclusions could be made to ensure that the effect is not due to a specific disposition of particles. For instance, some of the inclusions could be positioned so that they are intercepted by the plates; in this case, there would not be a layer that only consists of matrix at the aggregate-plate boundary.

References

Ahrens, J., Geveci, B., & Law, C. (2005). *ParaView: An End-User Tool for Large Data Visualization*. Elsevier.

Ayachit, U. (2015). *The ParaView Guide: A Parallel Visualization Application*. Kitware.

Barnes, H. (2000). *A handbook of elementary rheology*. The University of Wales Institute of Non-Newtonian Fluid Mechanics, University of Wales, Aberystwyth.

Bell, T. H., Rubenbach, M. J., & Fleming, P. D. (1986). Porphyroblast nucleation, growth and dissolution in regional metamorphic rocks as a function of deformation partitioning during foliation development. *Journal of Metamorphic Geology*, *4*(1), 37–67.

Einstein, A. (1906). Eine neue bestimmung der molekldimensionen. *Annalen der Physik*, *324*(2), 289–306.

Faccenda, M., & Dal Zilio, L. (2017). The role of solid-solid phase transitions in mantle convection. *Lithos*, *268-271*, 198–224.

Genovese, D. B. (2012). Shear rheology of hard-sphere, dispersed, and aggregated suspensions, and filler-matrix composites. *Advances in Colloid and Interface Science*, *171-172*, 1–16.

Gerya, T. V., & Yuen, D. A. (2007). Robust characteristics method for modelling multiphase visco-elasto-plastic thermo-mechanical problems. *Physics of the Earth and Planetary Interiors*, *163*, 83–105.

Girard, J., Amulele, G., Farla, R., Mohiuddin, A., & Karato, S.-i. (2016).

Shear deformation of bridgmanite and magnesiowustite aggregates at lower mantle conditions. *Science*, *351*(6269), 144–147.

Handy, M. R. (1994). Flow laws for rocks containing two non-linear viscous phases: A phenomenological approach. *Journal of Structural Geology*, *16*(3), 287–301.

Hirose, K. (2002). Phase transitions in pyrolitic mantle around 670-km depth: Implications for upwelling of plumes from the lower mantle. *Journal of Geophysical Research: Solid Earth*, *107*(B4).

Hsueh, C. H., & Wei, W. C. (2009). Analyses of effective viscosity of suspensions with deformable polydispersed spheres. *Journal of Physics D: Applied Physics*, *42*(7).

Jin, Z.-M., Zhang, J., Green, H., II, & Jin, S. (2001). Eclogite rheology: Implications for subducted lithosphere. *Geology*, *29*(8), 667.

Kaminski, É., Ribe, N. M., & Browaeys, J. T. (2004). D-Rex, a program for calculation of seismic anisotropy due to crystal lattice prefferred orientation in the convective upper mantle. *Geophysical Journal International*, *158*(2), 744–752.

Karato, S.-i., Wang, Z., Liu, B., & Fujino, K. (1995). Plastic deformation of garnets: systematics and implications for the rheology of the mantle transition zone. *Earth and Planetary Science Letters*, *130*(1), 13 – 30.

Karato, S.-i., & Weidner, D. J. (2008). Laboratory Studies of Rheological Properties of Minerals Under Deep Mantle Conditions. *Elements*, *4*, 191–196.

Kitano, T., Kataoka, T., & Shirota, T. (1981). An empirical equation of

the relative viscosity of polymer melts filled with various inorganic fillers. *Rheologica Acta*, *20*(2), 207–209.

Krieger, I. M., & Dougherty, T. J. (1959). A Mechanism for Non-Newtonian Flow in Suspensions of Rigid Spheres. *Transactions of the Society of Rheology*, *3*(1), 137–152.

Madi, K., Forest, S., Cordier, P., & Boussuge, M. (2005). Numerical study of creep in two-phase aggregates with a large rheology contrast: Implications for the lower mantle. *Earth and Planetary Science Letters*, *237*(1), 223 – 238.

Mancktelow, N. S., & Pennacchioni, G. (2005). The control of precursor brittle fracture and fluid-rock interaction on the development of single and paired ductile shear zones. *Journal of Structural Geology*, *27*(4), 645–661.

MATLAB Optimization Toolbox (2017). Matlab optimization toolbox. The MathWorks, Natick, MA, USA.

Moresi, L., Dufour, F., & Mhlhaus, H.-B. (2003). A lagrangian integration point finite element method for large deformation modeling of viscoelastic geomaterials. *Journal of Computational Physics*, *184*(2), 476 – 497.

Moulas, E., Burg, J. P., & Podladchikov, Y. (2014). Stress field associated with elliptical inclusions in a deforming matrix: Mathematical model and implications for tectonic overpressure in the lithosphere. *Tectonophysics*, *631*(C), 37–49.

Mueller, S., Llewellin, E. W., & Mader, H. M. (2010). The rheology of suspensions of solid particles. *Proceedings of the Royal Society of London A*, *466*(2116), 1201–1228.

Pennacchioni, G., Fasolo, L., Cecchi, M. M., & Salasnich, L. (2000). Finite-element modelling of simple shear flow in Newtonian and non-Newtonian fluids around a circular rigid particle. *Journal of Structural Geology*, *22*(5), 683–692.

Pennacchioni, G., & Mancktelow, N. S. (2007). Nucleation and initial growth of a shear zone network within compositionally and structurally heterogeneous granitoids under amphibolite facies conditions. *Journal of Structural Geology*, *29*(11), 1757 – 1780.

Ringwood, A. E. (1991). Phase transformations and their bearing on the constitution and dynamics of the mantle. *Geochimica et Cosmochimica Acta*, *55*(8), 2083–2110.

Rintoul, M. D., & Torquato, S. (1996). Computer simulations of dense hard-sphere systems. *The Journal of Chemical Physics*, *105*(20), 9258–9265.

Schmid, D. W., & Podladchikov, Y. Y. (2003). Analytical solutions for deformable elliptical inclusions in general shear. *Geophysical Journal International*, *155*(1), 269–288.

Stixrude, L., & Lithgow-Bertelloni, C. (2012). Geophysics of chemical heterogeneity in the mantle. *Annual Review of Earth and Planetary Sciences*, *40*(1), 569–595.

Takeda, Y. T. (1998). Flow in rocks modelled as multiphase continua: Application to polymineralic rocks. *Journal of Structural Geology*, *20*(11), 1569–1578.

Wang, Y., Hilairet, N., Nishiyama, N., Yahata, N., Tsuchiya, T., Morard, G., & Fiquet, G. (2013). High-pressure, high-temperature deformation of CaGeO3

(perovskite)±MgO aggregates: Implications for multiphase rheology of the lower mantle. *Geochemistry, Geophysics, Geosystems*, *14*(9), 3389–3408.

Yamazaki, D., & Karato, S. I. (2001). Some mineral physics constraints on the rheology and geothermal structure of Earth's lower mantle. *American Mineralogist*, *86*(4), 385–391.